Journal of Industrial and Engineering Chemistry 99 (2021) 364–379

Contents lists available at ScienceDirect

Journal of Industrial and Engineering Chemistry

journal homepage: www.elsevier.com/locate/jiec

Fe/olivine as primary catalyst in the biomass steam gasification in a fountain confined spouted bed reactor

M. Cortazar[a], L. Santamaria[a], G. Lopez[a,b,*], J. Alvarez[c], M. Amutio[a], J. Bilbao[a], M. Olazar[a]

[a] Department of Chemical Engineering, University of the Basque Country, UPV/EHU, P.O. Box 644, E48080 Bilbao, Spain
[b] IKERBASQUE, Basque Foundation for Science, Bilbao, Spain
[c] Department of Chemical and Environmental Engineering, University of the Basque Country, UPV/EHU, Nieves Cano 12, Vitoria, Gasteiz 01006, Spain

ARTICLE INFO

Article history:
Received 13 February 2021
Received in revised form 16 April 2021
Accepted 24 April 2021
Available online 28 April 2021

Keywords:
Biomass gasification
Spouted bed
Primary catalyst
Tar
Syngas

ABSTRACT

The performance of Fe/olivine catalysts was tested in the continuous steam gasification of sawdust in a bench scale plant provided with a fountain confined conical spouted bed reactor at 850 °C. Olivine was used as catalyst support and loaded with 5 wt%Fe. The activity and stability of the catalyst was monitored by nitrogen adsorption-desorption, X-ray fluorescence spectroscopy, temperature programmed reduction, X-ray diffraction and X-ray photoelectron spectroscopy techniques, which were conducted before and after the runs. The fountain confined conical spouted bed performs well in the biomass steam gasification with primary catalysts. In fact, this reactor allows enhancing the gas-solid contact, and therefore the catalytic activity by avoiding the elutriation of fine catalyst particles. The uncatalysed efficiency of the gasification process, assessed based on the gas production and composition, H_2 production, tar concentration and composition, and carbon conversion efficiency, was consideraby improved on the Fe/olivine catalyst, with tar reduction being especially remarkable (to 10.4 g Nm^{-3}). After 140 min on stream, catalyst deactivation was particularly evident, as tar concentration increased to 19.9 g Nm^{-3} (90% of that without catalyst). However, Fe/olivine catalyst was still active for WGS and CH_4 steam reforming reactions, with gas and H_2 productions being 1.35 Nm^3 kg^{-1} and 5.44 wt%, respectively. Metal iron oxidation to Fe_3O_4 caused catalyst deactivation, as the reaction environment shifted from oxidizing to reducing conditions due to operational limitations.

© 2021 The Author(s). Published by Elsevier B.V. on behalf of The Korean Society of Industrial and Engineering Chemistry. This is an open access article under the CC BY-NC-ND license (http://creativecommons.org/licenses/by-nc-nd/4.0/).

Introduction

In the current energy scenario, the production of heat, power and biofuels from biomass has become of major interest. In this line, gasification is a key technology for the large-scale exploitation of biomass. However, the development of biomass gasification is conditioned by the efficient conversion of the feed and the formation of troublesome by-products, such as tars [1–6].

The tar is a complex mixture of high molecular weight aromatic hydrocarbons, which cause fouling, corrosion and blocking of downstream equipment, leading to unacceptable level of maintenance for engines and turbines. Apart from the total concentration of the tar, its nature (mainly its dew point) also determines the problems associated with this matter. Nevertheless, the tar contains a significant amount of energy that could be transformed into syngas by acting on the operating conditions, reactor design and gas conditioning systems [7–12].

The design of conventional conical spouted bed reactors has recently been modified to optimize reactor performance, especially for biomass steam gasification. Conventional spouted bed reactors are characterized by short gas residence times, which is an advantage for pyrolysis processes, but a severe drawback for gasification ones because tar cracking/reforming reactions are avoided [13,14]. Thus, the fountain confined spouted bed reactor has been developed to overcome these problems and improve the overall process efficiency [15–17]. Moreover, this novel technology widens the applicability range of conventional spouted beds, as it may handle very fine particles without elutriation from the bed by confining in the fountain the gases produced in the bed, and therefore lengthening their path. Therefore, the gas residence time is increased and the gas-solid contact improved, which is even better under the fountain enhanced regime. The latter regime is characterized by a great expansion of the fountain region, which significantly improves the contact between the gas and the solid, and therefore tar conversion [18–21].

* Corresponding author at: Department of Chemical Engineering, University of the Basque Country, UPV/EHU, P.O. Box 644, E48080 Bilbao, Spain.
E-mail address: gartzen.lopez@ehu.eus (G. Lopez).

https://doi.org/10.1016/j.jiec.2021.04.046
1226-086X/© 2021 The Author(s). Published by Elsevier B.V. on behalf of The Korean Society of Industrial and Engineering Chemistry. This is an open access article under the CC BY-NC-ND license (http://creativecommons.org/licenses/by-nc-nd/4.0/).

Catalytic gas cleaning methods for tar removal also entail an additional increase in H_2 and gas productions, as they promote tar cracking and steam reforming reactions. These catalysts may be used as primary catalysts directly in the gasifier, or as secondary catalysts in downstream catalytic processes. Thus, in the case of fluidized bed reactors, the use of an active and appropriate in-bed material as primary catalyst is a promising strategy to decrease the tar content in comparison with the use of a more expensive secondary catalytic reactor downstream [22–28].

A large number of materials with significant activity for tar cracking and reforming have been used as primary catalysts. Natural minerals, such as dolomite and olivine, have attracted most of the attention because, apart from being active for tar cracking and reforming, they are inexpensive and abundant. Although the activity of dolomite is reported to overcome that of olivine, it is very fragile and undergoes severe attrition when used in fluidized beds. Furthermore, olivine has higher mechanical strength, comparable to that of sand [14,29–36]. However, the catalytic activity of these primary materials for tar conversion leaves room for improvement by metal phase addition.

Ni based catalysts are more effective for converting tar into hydrogen-rich gas, but they undergo a rapid deactivation by coke deposition and are toxic [37–44]. Recently, iron based catalysts have gained considerable attention among the catalysts for tar removal. Compared to nickel, the use of iron reduces the catalyst cost and lowers its toxicity [45–55]. Apart from the well-known activity of metallic iron for tar reforming and cracking, magnetite (Fe_3O_4) has also been proven to be active for the WGS reaction [56–58]. Therefore, impregnation of natural minerals with iron seems to be an interesting alternative to synthesize primary catalysts.

The novelty of this paper is associated with the proposal of a novel and efficient gasification technology. Thus, an original gasification technology based on the fountain confined spouted bed reactor has been developed. This reactor is able to operate under a vigorous fluidization regime (enhanced fountain regime), which greatly improves the gas-solid contact, and therefore the catalyst efficiency. Accordingly, this paper assesses the potential benefits of the fountain confined conical spouted bed for reducing the tar produced during biomass gasification, and the potential to improve the overall process efficiency by using Fe/olivine catalysts. Furthermore, the novelty is also related to the role of active iron species and their behaviour in biomass steam gasification. Thus, this paper analyses the performance and stability of an Fe/catalyst and relate its activity for biomass steam gasification with its physical and metallic properties. A detailed characterization (BET surface area, X-ray fluorescence (XRF), X-ray diffraction (XRD), X-ray photoelectron spectroscopy (XPS), temperature programmed reduction (TPR) and oxidation (TPO)) of the fresh and deactivated catalysts was carried out to ascertain the cause of the deactivation.

Experimental

Materials

The biomass feedstock used in this study was crushed and sieved forest pinewood sawdust with an average particle size of 1–2 mm and dried to a moisture content below 10 wt%. The ultimate and proximate analyses were conducted in a LECO CHNS-932 elemental analyzer and in a TGA Q5000IR thermogravimetric analyzer, respectively. Moreover, the higher heating value (HHV) was measured in a Parr 1356 isoperibolic bomb calorimeter. The main features of the biomass used are listed in Table 1.

Table 1
Pinewood characterization.

Ultimate analysis (wt%)[a]	
Carbon	49.33
Hydrogen	6.06
Nitrogen	0.04
Oxygen[b]	44.54
Proximate analysis (wt%)[c]	
Volatile matter	73.4
Fixed carbon	16.7
Ash	0.5
Moisture	9.4
HHV (MJ kg^{-1})	19.8

[a] On a dry basis.
[b] By difference.
[c] On an air dried basis.

Catalyst synthesis

Olivine supplied by Minerals Sibelco was used in this study as catalyst support and primary catalyst. Based on previous studies [19], olivine in the 90–150 μm particle size range was used in order to operate in the fountain enhanced regime. The performance of the Fe/olivine catalyst was compared with that of olivine, which was calcined in situ at 850 °C.

An Fe/olivine catalyst with 5 wt% iron was prepared by wet impregnation of the support with an aqueous solution of Fe $(NO_3)_3{\cdot}9H_2O$ (Panreac AppliChem, 98%), by means of a rotavapor, which allows evaporating the solution under reduced pressure and moderate temperatures. The rotavapor used was a *Büchi rotavapor R-114*, which operates under vacuum at 70 °C. A relatively low metallic load (5 wt%) was used, as the physical properties of olivine hinder a suitable dispersion of the metal due to its non-porous nature. The iron solution was added to the support and the water excess was evaporated at 70 °C and under vacuum environment. The samples were dried in an oven at 100 °C for a couple of days and calcined in a muffle oven at 1000 °C for 4 h.

Characterization techniques

The physical properties of the catalyst (specific surface area, pore volume and average pore size) were determined by N_2 adsorption–desorption in a Micromeritics ASAP 2010 apparatus. Before each analysis, the samples were degassed under vacuum at 150 °C overnight. Surface area was calculated based on the BET equation, whereas the pore size distribution was determined by BJH method.

X-ray fluorescence (XRF) spectrometry was used to measure the chemical composition (wt%) of both the calcined olivine and the synthesized catalyst. The chemical analysis of the particles was carried out under vacuum atmosphere using a sequential wavelength dispersion X-ray fluorescence (WDXRF) spectrometer (Axios 2005, PANalytical) equipped with a Rh tube, and three detectors (gaseous flow, scintillation and Xe sealing). The calibration lines were determined by means of well-characterized international patterns of rocks and minerals.

X-ray powder diffraction (XRD) patterns were obtained in a Bruker D8 Advance using CuKα radiation equipped with a Germanium primary monochromator and Sol-X dispersive energy detector in order to analyze the crystalline structure of both the olivine and the reduced catalyst. The spectra were obtained in a 2θ range of 20–90°. The diffraction spectra were indexed by comparing with JCPDS files (Joint Committee on Powder Diffraction Standards).

X-ray photoelectron spectroscopy (XPS) analysis was carried out to record in detail the elements making up the surface, and quantify and analyze their oxidation states. XPS measurements were conducted in a SPECS system equipped with a Phoibos 150 1D-DLD analyzer and a monochromatic Al-Kα radiation source (1486.7 eV). Prior to the analysis, the spectrometer was calibrated with Ag (Ag $3d^5$/2368.26 eV).

The reducibility of the materials was determined by Temperature Programmed Reduction (TPR) in an AutoChem II 2920 Micromeritics. The tests were carried out on a 200 mg sample, through which a flow of 10 vol% hydrogen in argon was circulated. Prior to the reduction experiments, the catalyst was thermally treated under He stream at 200 °C in order to remove water or any impurities. The temperature was increased at a rate of 10 °C min^{-1} from room temperature to 900 °C. A thermal conductivity detector (TCD) was used to analyze the hydrogen consumption of the samples and its signal recorded continuously.

Carbon deposition on the catalyst was ascertained by temperature programmed oxidation (TPO) in a Thermobalance (TGA Q5000 TA Instruments) coupled in-line to a mass spectrometer (Thermostar Balzers Instrument). This device allows recording the signals at 14, 18, 28 and 44 atomic numbers, corresponding to N_2, H_2O, CO and CO_2, respectively. The coke content was determined based on CO_2 signal. Once the signal was stabilized under N_2 stream (50 mL min^{-1}) at 100 °C, oxidation of the sample with air was carried out by increasing temperature to 800 °C using a ramp of 5 °C min^{-1} and keeping the final temperature for 30 min to ensure total carbon combustion.

Experimental equipment

The biomass steam gasification experiments were performed in a bench scale unit based on the conical spouted bed technology (Fig. 1). This reactor was designed for biomass valorization processes, and specifically fine-tuned and optimized for the pyrolysis and gasification of different solid wastes [59–63].

The main element of the plant is a fountain confined conical spouted bed, which is also provided with a non-porous draft tube (internal diameter 5.5 mm and entrainment zone height 15 mm). It enables operating in a wide range of conditions and improving the hydrodynamic performance of the reactor. This reactor may also operate in the conventional spouting regime by using a lid without confiner. The main dimensions of the reactor are as follows: cylindrical section diameter 95 mm, height of the conical section 150 mm, cone included angle 30°, length of the fountain confiner 330 mm, and total height of the reactor 430 mm. The cone base diameter is 20 mm, and the internal diameter of the fountain confiner 54 mm, with its volume being of around 0.8 L. The height from the reactor base to the lower end of the confiner is 105 mm. The fountain confiner is a tube welded to the lid of the reactor, whose lower end is close to the bed surface and confines the gases generated in the bed and force them to circulate upwards through the core of the fountain and downwards through its periphery. This device increases the residence time, narrows its distribution and enhances gas-solid contact in the fountain region [17]. Furthermore, the draft tube makes operation feasible in a much wider range of gas flowrates and improves bed stability [64]. More details about the reactor, fountain confinement technology and draft tube have been reported elsewhere [18,19]. A gas preheater is located below the reactor to heat the gases to reaction conditions. A radiant oven made up of two independent sections heats the gasifier (the lower section heats the gas preheater and the upper section the fountain confined spouted bed reactor). The temperature in each section is controlled by two thermocouples, one placed in the bed annulus and the other one at the inlet of the gaseous stream.

All the unit elements, i.e., the reactor, the interconnection pipes, the cyclone and the filter, are located inside a forced convection oven, which is 1830 × 1950 × 1000 mm stainless steel box and features 100 mm insulation of quartz wool with fiberglass reinforcement fabric, kept at 300 °C to prevent tar condensation before the condensation system. The high-efficiency cyclone and 5 μm sintered steel filter retain the char and catalyst fine particles entrained from the bed.

The biomass was fed by means of a piston dispenser. This system consists of a cylindrical vessel equipped with a vertical shaft connected to a piston placed below the material bed. When the piston rises, the biomass is pushed towards the top of the feeding system and drops into the reactor through a tube cooled with tap water at the same time as the whole system is vibrating by means of an electric engine to prevent biomass agglomeration. Moreover, a very small nitrogen flow is introduced from the top of the feeding vessel in order to ease the solid flow into the reactor and avoid the condensation of steam in the dispenser. A detailed description of the functioning of this device to feed the solid has been reported elsewhere [20]. The water flowrate was measured

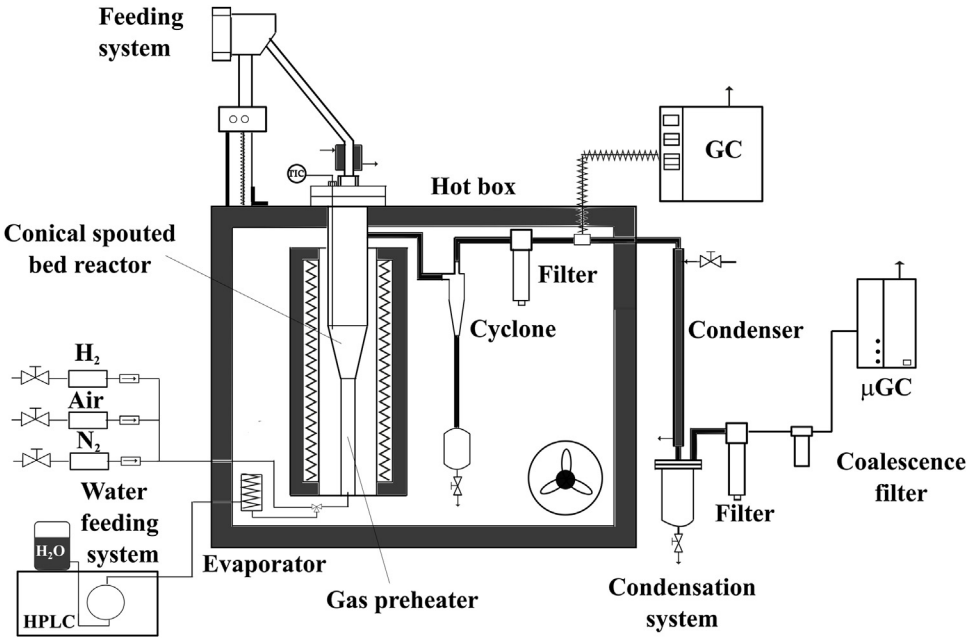

Fig. 1. Experimental bench scale pilot plant.

by an ASI 521 pump and directed to an evaporator to produce steam before entering the reactor. The plant is also provided with three mass flow meters for N_2, air and H_2, with N_2 being used as fluidizing agent during the heating process and H_2 for the reduction of Fe catalyst prior to the runs.

The volatile condensation system is located after the convection oven and consists of a double-shell tube condenser cooled by tap water, a 1 L vessel, a stainless steel filter (60 μm) and a coalescence filter, with the latter ensuring total recovery of the tars.

Operating conditions

Continuous gasification experiments were performed at 850 °C using steam as fluidizing gas. Thus, a water flow rate of 1.5 mL min^{-1} was employed (1.86 NL min^{-1} of steam) and biomass was fed at a rate of 0.75 g min^{-1}, which corresponded to a steam/biomass (S/B) ratio of 2. This high S/B ratio is needed to guarantee vigorous spouting conditions (enhanced fountain regime), as steam not only acts as gasifying agent, but also as fluidizing gas.

The bed consisted of 100 g either calcined olivine or Fe/olivine catalyst, with their particle size being in the 90–150 μm range. Prior to the reactions, the iron catalyst was subjected to an in situ reduction process at 850 °C for 4 h with a stream containing 10 vol% of H_2 to ensure complete reduction to Fe^0 phase.

The experiments were performed in continuous regime and the gas chromatography (GC) and micro GC analyses were conducted once several minutes of operation had elapsed to ensure steady state conditions. Moreover, the runs were repeated several times (at least three) under the same conditions in order to guarantee reproducibility of results.

Certain limitations in the experimental unit for operation and product monitoring had to be addressed. Thus, the feeder must be refilled after 40 min operation and the GC analysis of the tars lasts about 20 min. Accordingly, successive 10 min reactions were carried out in order to ensure suitable product analysis throughout continuous operation and overcome these limitations.

Product analysis

Samples of the volatile stream leaving the reactor were analysed on-line by means of a GC Agilent 7890 outfitted with a HP-Pona column (50 m long, 0.2 mm in internal diameter and a coating thickness of 0.5 mm) a flame ionization detector (FID). The sample was injected into the GC through a line thermostated at 280 °C to avoid the condensation of the tars. The temperature programme used in the GC is as follow: 2 min at 40 °C in order to attain a good separation; a sequence of 25 °C min^{-1} up to 320 °C and 7 min at this temperature to ensure that all products were outside the column. Furthermore, the non-condensable gaseous stream was also analysed online in a Varian 4900 micro GC equipped with three modules (molecular sieve, Porapak (PPQ) and plot alumina) and thermal conductivity detectors (TCD), which allow both identification and quantification of gaseous products previously calibrated. The conditions for the analysis were the same for the modules: column temperature 90 °C, injector temperature 100 °C and pressure 20 psi. In this case, the sampling point was located after the condensation and filtering sections. Moreover, the tars retained in the condensation system were identified by Shimadzu UP-2010 S GC/MS once they had been dissolved in acetone.

Reaction indexes

In order to assess the gasification performance the following reaction parameters were considered:

- Gas production (P_{gas}, $Nm^3\,kg^{-1}$) based on the mass unit of biomass fed into the gasification process:

$$P_{gas} = \frac{Q_{gas}}{m_0} \quad (1)$$

where Q_{gas} is the volumetric flow rate of the gas produced and m_0 is the mass flow rate of biomass fed into the process.

- H_2 production (P_{H_2}, wt%) by mass unit of the biomass fed into the reactor, which is calculated as follows:

$$P_{H_2} = \frac{m_{H_2}}{m_0} \cdot 100 \quad (2)$$

where m_{H_2} and m_0 are the mass flow rates of the H_2 produced and biomass fed into the reactor, respectively.

- Tar concentration determined as the amount of tar (in mass) per m^3 of syngas:

$$\text{Tar concentration}: \quad \frac{m_{tar}}{Q_{gas}} \quad (3)$$

- Carbon conversion efficiency defined as the ratio between the moles of C in the gaseous product and those entering the reactor.

$$(4) X = \frac{C_{gas}}{C_{biomass}} \cdot 100$$

Results

Catalyst characterization before tests

Table 2 shows the specific surface area, pore volume and average pore size. As observed, the specific surface area of the calcined olivine was as low as 1.92 $m^2\,g^{-1}$ and the pore volume 0.0023 $cm^3\,g^{-1}$, which are evidences of its non-porous structure. Regarding the synthesized Fe/olivine catalyst, olivine physical properties were improved by iron impregnation. Thus, pore volume and average pore size became larger, which was due to the collapse of the inter-pore structure of olivine. Likewise, the specific area also increased, which may be attributed to the deposition of Fe on the external surface. This trend has also been reported for Ni impregnation on low porosity surfaces [65,66].

The chemical compositions of the calcined olivine and the prepared catalyst are summarized in Table 3. The content of Fe in the olivine was of around 5.2 wt%. After impregnation, Fe content in the catalyst increased significantly, 10.2 wt%, which confirmed that the metal content was that corresponding to the impregnation (5 wt%) plus that in the original olivine.

Fig. 2 shows the diffractograms of the calcined olivine and fresh and reduced Fe/olivine. In the case of the calcined olivine, the XRD data revealed the main diffraction lines were characteristic to the olivine structure ($(Mg_{1.81}\cdot Fe_{0.19})\cdot(SiO_4)$). Additional peaks corresponding to secondary crystalline phases may also be observed, such as enstatite ($MgSiO_3$) and quartz (SiO_2). According to Michel et al. [67,68] and Świerczyński et al. [69], numerous phases of iron oxide may appear subsequent to olivine calcination, as are γ-Fe_2O_3, α-Fe_2O_3, Fe_3O_4 and $MgFe_2O_4$. The presence of these iron oxides is explained by the migration of the iron Fe^{2+} located within the

Table 2
Physical properties of the calcined olivine and Fe/olivine catalyst.

Catalyst	S_{BET} ($m^2\,g^{-1}$)	V_{pore} ($cm^3\,g^{-1}$)	d_{pore} (Å)
Olivine	1.92	0.0023	48.85
Fe/olivine	3.75	0.0076	80.85

Table 3
Chemical composition (wt%) of the calcined olivine and the Fe/olivine catalyst.

Component (wt%)	MgO	SiO_2	Fe_2O_3	CaO	Al_2O_3	Na_2O	TiO_2	MnO
Olivine	45.98	42.10	7.52	0.11	0.10	0.07	0.03	0.11
Fe/olivine	42.08	38.68	14.71	0.12	0.24	0.06	0.02	0.10

internal structure of the olivine to its surface due to oxidation (Eq. (5)) [69,70]. However, none of these phases were detected in this study. It should be noted that the calcination temperature used for the natural olivine was rather low (850 °C) compared to other studies in the literature, in which they were over 1100 °C. Kuhn et al. [71] performed XRD analysis to olivine calcined at 900 °C during 2 h and they neither observed free Fe oxide phases. These oxide phases diffract in the same main lines as the olivine structure, but they were not strong enough to be detected and so inferred their presence. For the fresh and reduced Fe/olivine catalysts, the main crystalline forms were still those corresponding to olivine structure and $MgSiO_3$ enstatite phase, even though the olivine was subjected to iron impregnation, calcination and reduction. However, significant changes in the relative intensity of olivine structure and $MgSiO_3$ enstatite phases were noticed at $2\theta = 21°$, 31° and 36°, which indicated certain modifications in the crystallinity of the samples due to iron impregnation. In fact, the higher intensity of the diffraction lines in the reduced catalyst is evidence of its greater crystallinity compared to the calcined olivine or fresh catalyst, which was due to iron reincorporation into the olivine structure. In addition, hematite (α-Fe_2O_3) peak appeared at $2\theta = 24°$ in the fresh catalyst, whereas for the reduced catalyst the presence of an intense peak of the metallic iron phase was observed at $2\theta = 44°$ and a smaller one at $2\theta = 65°$. Iron oxide phases were not detected in the reduced sample, which is evidence of their full reduction. Other authors reported the same main lines for this catalyst [47,48,72]. The SiO_2 lines detected in the support disappeared in the catalyst. Michel et al. [67] stated that olivine phase reacts with quartz at 1000 °C to form enstatite phase:

$$(Mg,Fe)_2SiO_4 + O_2 \rightarrow xMg_2SiO_4 + (1-x)SiO_2 + (2x-1)Fe_2O_3(\alpha) + 2(1-x)MgFe_2O_4 \quad (5)$$

Fig. 3 shows the XPS spectra for the samples in different binding energy ranges. This analysis revealed the main components on the surface of the samples, which were Si, Mg, Fe and O. No significant changes were observed in Si after iron impregnation and catalyst reduction, whereas more pronounced changes were detected in the peaks corresponding to Mg and Fe. In the case of Fe, its oxidation states are analyzed below in the paper. These variations are also visible in Tables 4 and 5. Furthermore, peaks of other trace elements, previously detected by XRF, were not observed, which is evidence that they were not located on the surface.

Table 4 shows the surface composition of the samples. The quantification of each element was carried out by integrating the intensities of Si 2p, Mg 2p, O 1s and Fe 2p using Scofield sensitivity factors. As observed, after iron impregnation, the amount of iron on the catalyst surface increased (from 6.2 to 8%), which suggests that part of the impregnated iron was deposited on the surface of the catalyst, as evidenced by the increase in the BET surface of the catalyst (Table 2). However, the amount of Mg on the surface decreased (from 17.5 to 14.2%) after iron loading. According to Frekdisson et al. [73], after the oxidizing treatments, the surface is enriched in Fe at the expense of Mg. Furthermore, catalyst reduction with H_2 led to a decrease in the amount of Fe to 4.4% and an increase in that of Mg to 22.1% on the surface. Under reducing conditions, Fe clustered into large particles and incorporated into the olivine structure [71]. Regarding oxygen concentration, its oscillations on the surface of the catalyst were related to the oxidation state of iron.

XPS spectra in the 700–750 eV binding energy range of the samples were analyzed to further understand the valence state of the iron in the calcined olivine and fresh and reduced Fe/olivine catalysts (Fig. 3b and c). Accordingly, Fe 2p lines were used instead of Fe 3p because they were stronger. Moreover, Table 5 shows the iron distribution on the surface of the samples. Yamashita and Hayes [74] reported that Fe $2p_{3/2}$ peak at 711 eV with satellite peak at 719 eV and Fe $2p_{1/2}$ peak at 725 eV with satellite peak at 732 eV are characteristic of Fe^{3+}, whereas Fe $2p_{3/2}$ peak at 709 eV with satellite peak at 714 eV and Fe $2p_{1/2}$ peak at 723 eV with satellite peak at 728 eV correspond to Fe^{2+}. In Fig. 3c, the positions of these peaks are marked with dashed lines. Iron in Fe^{3+} state corresponds to Fe_2O_3 and $MgFe_2O_4$ compounds, whereas Fe^{2+} state is characteristic of iron in the olivine structure and FeO. In the calcined olivine, most of the Fe was as Fe^{3+} and doubled the amount of Fe as Fe^{2+}, which is evidence that a higher amount of iron led to free oxides on the surface than those remained within the olivine structure. The presence of free iron oxide phases (Fe^{3+}) stemmed from Fe migration from the olivine structure (Fe^{2+}) during the calcination process [69,73], although none of these compounds were detected by XRD analysis. Regarding iron

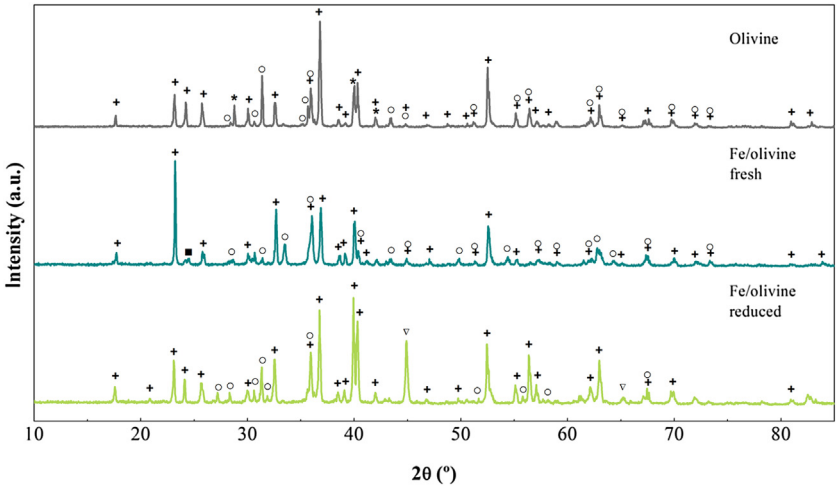

Fig. 2. XRD patterns of the calcined olivine and fresh and reduced catalysts. Crystalline phases: (+) $((Mg_{1.81}\cdot Fe_{0.19})\cdot(SiO_4))$, (o) $MgSiO_3$, (*) SiO_2, (■) Fe_2O_3, (▽) Fe^0.

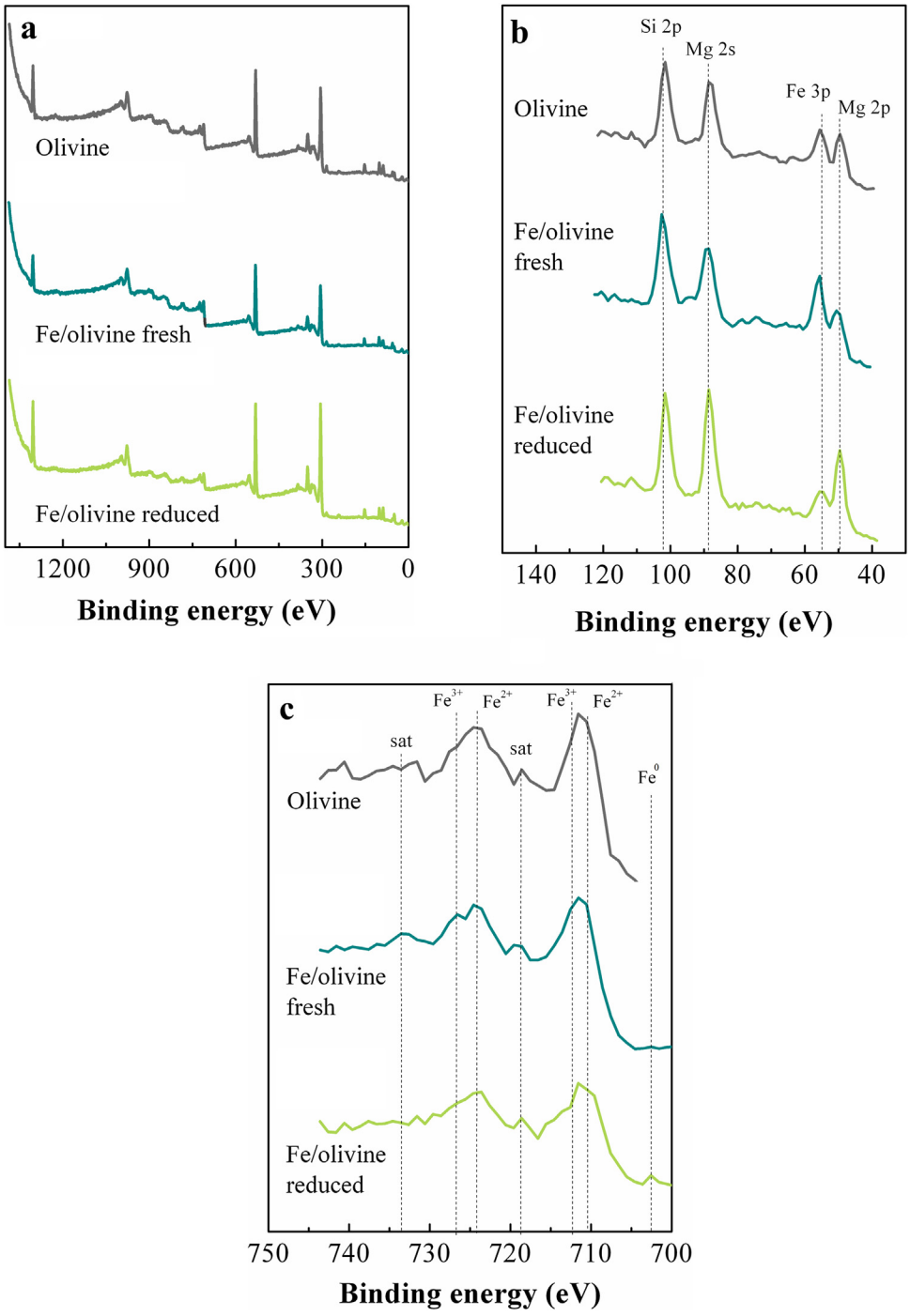

Fig. 3. Wide XPS spectra (a), XPS spectra for low binding energy regions (b) and XPS spectra for Fe 2p (c) of the calcined olivine, and fresh and reduced Fe/olivine catalysts.

distribution, the fresh Fe/olivine catalyst followed the same trend as the calcined olivine. However, when the former is compared with the calcined olivine, the amount of Fe^{2+} in the fresh catalyst increased (from 32. 89 to 35.42%), whereas that of Fe^{3+} decreased (from 67.11 to 64.54%), although Fe^{2+}/Fe^{3+} ratio remained approximately constant. These results suggest that, after impregnation, the iron within the olivine structure was preferably in the metallic state rather than forming free oxides. After reduction, a weak peak of metallic Fe appeared at 707 eV, which cannot be quantified due to its very small size. It seems that the metallic iron on the catalyst surface was oxidized due to its contact with air, but the iron inside the olivine remained in the metallic form, as was revealed by the XRD analysis (Fig. 2). Moreover, the Fe^{2+}/Fe^{3+} ratio in the reduced catalyst was higher than that in the fresh one, with the amount of Fe^{2+} and Fe^{3+} being almost the same. Thus, the oxidation state of the iron located on the surface changed from a Fe^{3+} dominating state after oxidation to Fe^{2+} state after reduction

Table 4
Surface composition (%) of the calcined olivine and Fe/olivine catalysts determined by XPS.

Component	Si	Mg	O	Fe
Olivine	15.8	17.5	60.6	6.2
Fe/olivine fresh	15.1	14.2	62.7	8.0
Fe/olivine reduced	14.6	22.1	58.9	4.4

Table 5
Iron distribution (%) on the surface of the calcined olivine and fresh and reduced Fe/olivine catalysts determined by XPS.

	Fe^{2+}	Fe^{3+}
Olivine	32.89	67.11
Fe/olivine fresh	35.42	64.58
Fe/olivine reduced	48.95	51.05

[73]. Meng et al. [72] observed the same trend for the iron distribution on the surface of the catalyst.

H_2-TPR experiments for the bed materials were carried out prior to their use in the reaction environment. The TPR profile of the catalysts enables determining the temperature needed for their reduction [75]. As well-known, the profile depends not only on the nature of the metallic species, but also on the metal-support interactions. Moreover, as the metallic iron is supposed to be the active phase for hydrocarbon cracking, the reducibility of the catalysts is of great relevance [76].

The TPR profiles of the calcined olivine and synthesized catalyst are shown in Fig. 4. In the case of the calcined olivine, two small peaks are observed between 350 and 550 °C. A third peak is also observed at a reduction temperature above 600 °C. In the case of the first two peaks, their low reduction temperature is evidence that these species are easy to reduce. Thus, these peaks are attributed to the reduction of iron oxides on the olivine surface [77]. According to the XPS analysis (Table 5), the surface of the calcined olivine is presumably made up of Fe_2O_3 and/or $MgFe_2O_4$, which migrated from the internal olivine structure during the calcination [48,69,71,72]. Thus, the peak at 350 °C is assigned to the reduction of Fe_2O_3 and the peak at 550 °C to the reduction of Fe_3O_4, as the reduction of Fe_2O_3 to metallic Fe occurs in two steps ($Fe_2O_3 \rightarrow Fe_3O_4 \rightarrow Fe^0$) [46,48]. The peak that might appear at higher temperatures is associated with the reduction of iron phases inside the olivine grain, in which reduction is more difficult. The TPR profile of the Fe/olivine catalyst shows a broad reduction zone covering the range from 300 to 700 °C. Three main peaks may be observed, with the first two being associated with the two-step oxidation of Fe_2O_3 on the olivine surface and the peak above 600 °C to the Fe atoms that migrated into the olivine support to form a very stable $MgFe_2O_4$ spinel phase [78]. In the case of the Fe/olivine catalyst, the reduction of iron phases inside the olivine grain is not observed due to the high stability of the olivine structure, i.e., higher temperatures are required for its reduction.

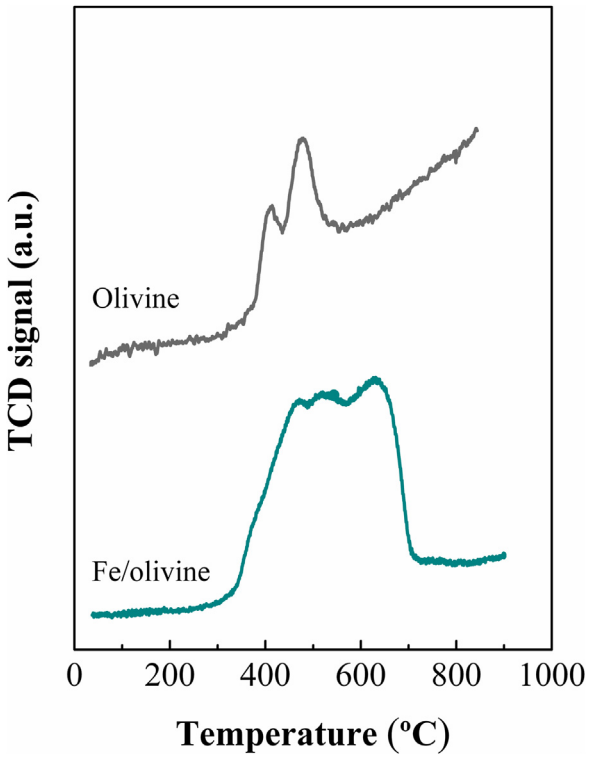

Fig. 4. TPR profiles of the catalysts.

Evaluation of the in-bed catalysts (zero time on stream)

The effect of Fe/olivine catalyst on the steam gasification process parameters (H_2 and gas productions, gas composition, carbon conversion and tar concentration and composition) was assessed and compared with that of calcined olivine. The performance of these in-bed materials was analyzed based on the following reactions inside the gasifier:

$$\text{Biomass pyrolysis}: \quad Biomass \rightarrow Gases(CO, CO_2, CH_4, H_2, \ldots) + oxygenates + char \tag{6}$$

$$\text{Steam gasification of the char}: \quad C(s) + H_2O \rightarrow CO + H_2 \tag{7}$$

$$CO_2\text{gasification of the char}: \quad C(s) + CO_2 \rightarrow 2CO \tag{8}$$

$$\text{Tar cracking}: \quad Tar \rightarrow CO + H_2 + CO_2 + C + CH_4 + \cdots \tag{9}$$

$$\text{Tar steam reforming}: \quad Tar + H_2O \rightarrow CO + H_2 \tag{10}$$

$$\text{Water gas} - \text{shift(WGS)}: \quad CO + H_2O \Leftrightarrow CO_2 + H_2 \tag{11}$$

$$\text{Methane(or hydrocarbon)steam reforming}: \quad CH_4 + H_2O \Leftrightarrow CO + 3H_2 \tag{12}$$

As observed in Fig. 5, all representative gasification parameters were significantly improved on the Fe/olivine catalyst. An increase in gas and hydrogen productions and a decrease in tar concentration was noticeable when 5 wt%Fe/olivine was used instead of olivine (Fig. 5a and b). Thus, gas production increased from 1.30 to 1.46 $Nm^3\,kg^{-1}$ and so did the hydrogen production, from around 5 wt% on the olivine to 6.25 wt% on the iron impregnated catalyst. Fig. 6 illustrates the product gas composition for the runs using 5 wt%Fe/olivine catalyst and calcined olivine. Iron impregnation led to an increase in H_2 concentration from 43.2 to 48.2 vol% and a reduction in that of CO, which implies that H_2/CO ratio increased from 1.41 for olivine to 3.26 for the iron catalyst. Consequently, CO_2 concentration increased to 28.2 vol%. From these results, it could be deduced that the addition of iron to olivine enhances the WGS reaction (Eq. (10)), as well as light hydrocarbon steam reforming and cracking reactions (Eqs. (8) and (11)). Consequently, tar concentration was reduced approximately to half, from 20.6 to 10.4 g Nm^{-3}, and carbon conversion efficiency accounted for 87.6% (Fig. 5c and d). Likewise, the heating value of the gas increased from 2.44 MJ m^{-3} with calcined olivine to 8.66 MJ m^{-3} with 5 wt% Fe/olivine catalyst. According to several authors [73,76,79], the metallic Fe on the reduced catalyst enhances tar decomposition reactions. Moreover, the BET surface area (Table 2) and XPS analyses (Table 4) revealed that Fe was mainly located on the external surface of the catalyst, and was therefore easily accessible to the volatiles and promotes tar cracking and reforming reactions (Eqs. (8) and (9)).

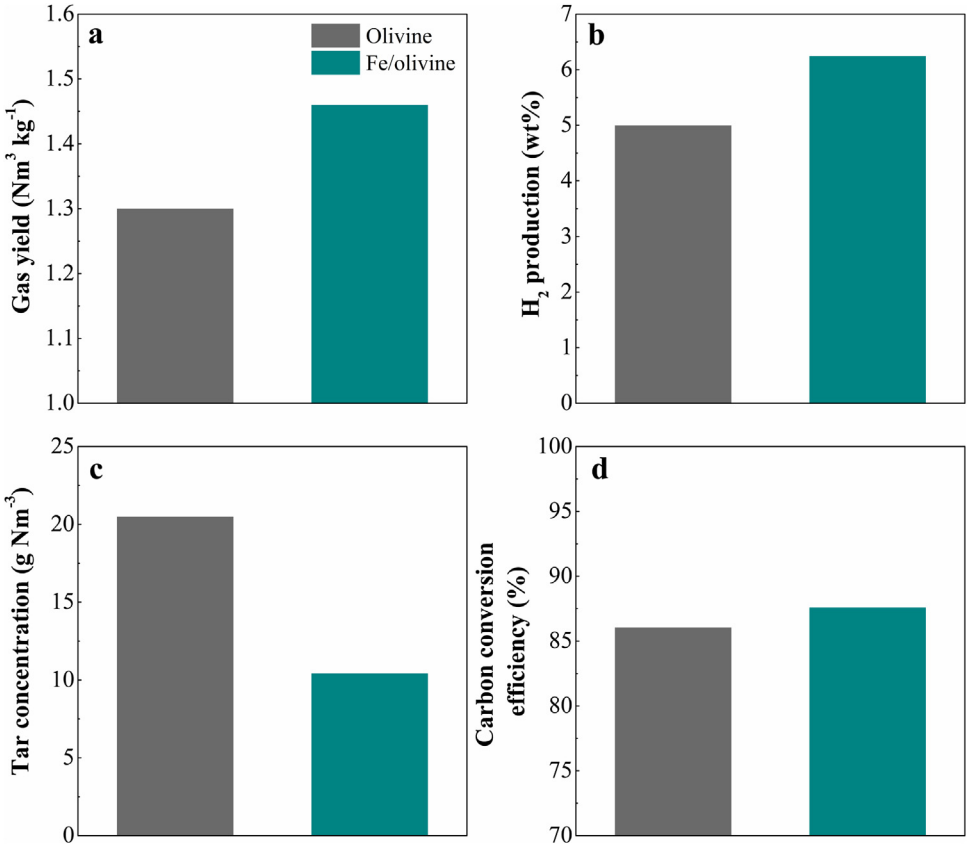

Fig. 5. Influence of iron impregnation on the gas production (a), H_2 production (b), tar concentration (c) and carbon conversion efficiency (d).

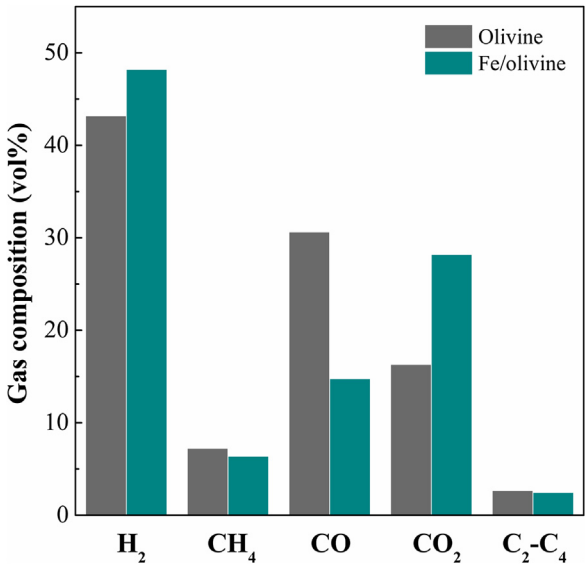

Fig. 6. Influence of iron impregnation into olivine on gas composition.

Although there are many studies dealing with steam reforming of biomass tar model compounds using a wide variety of supported metal catalyst [80–89], those dealing with the effect of metal impregnated in situ catalysts on the biomass steam gasification are scarce, especially those carried out in laboratory pilot plants. Several authors reported the same trend as that obtained in this study for iron impregnated olivine and compared its activity with that of raw olivine using different gasification technologies [45,49,50,90,91]. Thus, Rapagnà et al. [49] studied the performance of 10 wt%Fe/olivine catalysts in the biomass steam gasification at 820 °C in a fluidized bed gasifier and obtained slightly higher reaction indices than in this study. They observed that H_2 and gas productions increased from 3.5 to 6.6 wt% (the gaseous stream contained 53 vol% of H_2) and from 1 to 1.4 $Nm^3 kg^{-1}$, respectively when an Fe/olivine catalyst was used instead of raw olivine, whereas tar concentration was reduced by approximately 62%, with the value being 2.25 g Nm^{-3} with the catalyst. Carbon conversion efficiency reached a value of 80%, which was similar to that obtained with raw olivine. Virginie et al. [50] used the same catalyst as the previous authors, but they used a dual fluidized bed. They reported that tar reduction was more notable in the presence of Fe/olivine in the bed than in the run with raw olivine (5.1 and 2.6 g Nm^{-3} of tar content for olivine and Fe/olivine at 850 °C). In addition, Barisano et al. [90,91] evaluated the performance of 10 wt %Fe/olivine catalyst in the biomass steam/O_2 gasification at 890 °C in an internal circulating bubbling fluidized bed (ICBFB) and they reported 1.2 $Nm^3 kg^{-1}$ and 3 wt% for the gas and H_2 productions, respectively. They also reported a reduction in the total tar content by 38% (from 10.1 to 6.2 g N m^{-3}), and 98% of carbon conversion efficiency was therefore attained. However, Pan et al. [45] used a lower Fe load in the catalyst (5 wt%Fe/olivine) for the steam co-gasification of pine sawdust and bituminous coal in a pyrolysis-reforming-combustion decoupled triple bed system (DTBG) at 850 °C. All the studied reaction indices were improved, but the differences were not as remarkable as those observed for the biomass steam gasification. Thus, they obtained gas and H_2 productions of 0.66 $Nm^3 kg^{-1}$ and 2.49 wt% (10% higher in both cases) and a tar content as low as 4.87 g Nm^{-3} (17% reduction).

Ni loading to olivine also enhances tar reforming activity in the biomass steam gasification, with the performance being even

better than that of Fe/olivine catalyst. Thus, Pfeifer et al. [92] studied tar removal activity of Ni/olivine catalyst in a 100 kWth dual fluidized bed reactor. After adding 20% of 5 wt%Ni/olivine catalyst to a bed of olivine, the tar concentration was reduced by half and gas and H_2 productions increased to 1 $Nm^3 kg^{-1}$ and 3.93 wt%, respectively at 850 °C. Michel et al. [93] used in situ 3.9 wt%Ni/olivine catalyst in the biomass steam gasification carried out in fluidized bed at 800 °C and reported a higher efficiency of the catalyst compared to raw olivine. Thus, they obtained H_2 and gas productions of 7.56 wt% and 1.7 $Nm^3 kg^{-1}$, instead of 3.36 wt% and 1 $Nm^3 kg^{-1}$ with olivine, and less than 1 wt% of tar. More recently, Tursun et al. [94] used 5 wt%Ni/olivine catalyst in a decoupled triple bed gasification system consisting of a pyrolyzer, reformer and combustor, and reported that the catalyst not only improved tar removal, but also enhanced H_2 and gas productions. Their results were slightly better than those obtained by Michel et al. [93], but the Ni loading was also slightly higher. They reported a gas production of 1.59 $Nm^3 kg^{-1}$, with H_2 concentration being 56.1 vol% (H_2 production of 7.96 wt%) and tar content as low as 0.6 g Nm^{-3}.

The tar fraction is a mixture containing polycyclic aromatic compounds larger than benzene, and is commonly studied by dividing into four lumps [7], as are: light aromatics (monoaromatic compounds), heterocycles (aromatic rings with heteroatoms), light polyaromatics (PAHs with up to 3 rings) and heavy polyaromatics (PAHs with more than 3 rings). Apart from the total concentration of the tar, its nature (mainly its dew point) is of high relevance, as it is responsible of problems related to fouling and sooting.

Fig. 7 shows a significant reduction in the amount of heterocycles and heavy PAHs using Fe/olivine catalyst. In fact, the mass fraction of those lumps was reduced from 10.33 and 10.20 to 7.43 and 5.05 wt%, respectively. However, the percentage of light aromatics and PAHs in the total tar amount increased from 14.22 and 62.09 to 19.91 and 65.20 wt%. It is noteworthy that the Fe/olivine catalyst managed to reduce significantly the concentration of all tar families, as shown in Table 6. Based on the tar formation and PAH growth mechanisms [95], the Fe/olivine catalyst seems to hinder the growth of light PAHs into heavier ones, and the amount of the light PAHs was therefore higher. Furthermore, Diels–Alder reactions involving light alkenes in the permanent gases and phenols may produce light aromatics, and therefore its amount was increased [96–98].

Table 6 provides a detailed composition of the tar obtained with raw olivine and Fe/olivine catalyst. Naphthalene was the most abundant tar molecule for calcined olivine and Fe/olivine catalyst, although its concentration was reduced by 42% approximately with the iron enrich catalyst. Barisano et al. [91] reported a higher naphthalene reduction (of around 58%) in the biomass steam/O_2 gasification. Moreover, compounds such as phenol, methyl phenol, 1-methyl naphthalene, dibenzofuran, 1-H phenalene, 2-phenyl naphthalene and pirene were significantly removed, as the catalyst managed to reduce their content beyond 60%. Thus, it is clear that metallic iron is active for C—C and C—H bond breakdown [76,99]. The results in Table 6 also show the more stable tar compounds, which are those that are more difficult to remove. Using the Fe/olivine catalyst the concentration of toluene, naphthalene and anthracene was reduced, but their amounts were still rather high, as they are refractory to reforming/cracking reactions [49]. Therefore, all the efforts in the development of supported metal catalysts should be directed towards their capacity for removing the most stable tar compounds.

Stability of the Fe/olivine catalyst

The evolution of the gasification performance (Fig. 8) and gas and tar compositions (Figs. 9 and 10) were monitored for Fe/olivine with time on stream. In the case of the calcined olivine, gasification performance remained stable after 140 min on stream. The main properties of the Fe/olivine catalyst and their role on the biomass steam gasification explain these results.

Fig. 8 illustrates the evolution of the reaction indexes as a function of time on stream for Fe/olivine catalyst. Even though the performance of the calcined olivine remained stable after 140 min on stream, that of Fe/olivine catalyst underwent deactivation and the efficiency of the gasification process decreased with time on stream. Catalyst deactivation was especially evident by tar concentration, which increased by around 90%, from 10.4 to 19.8 g Nm^{-3}, as shown in Fig. 8c. After 140 min on stream, the amount of tar produced with the Fe/olivine catalyst reached almost that obtained with the calcined olivine (20.6 g Nm^{-3}). Other reaction indexes also showed the deterioration of the catalyst.

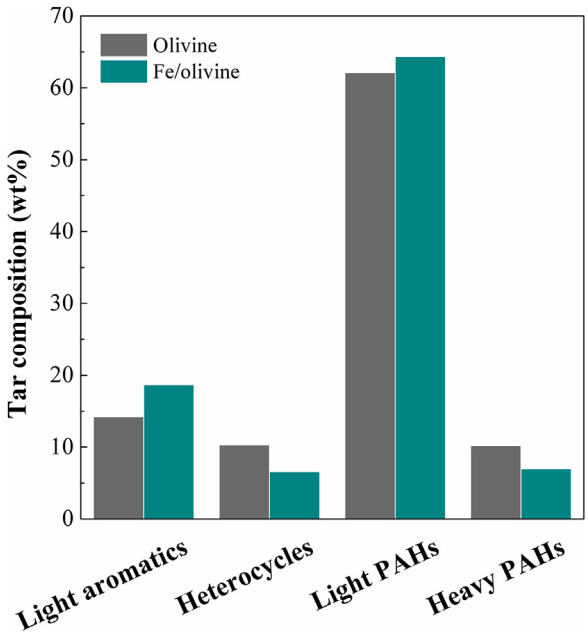

Fig. 7. Influence of iron loading on tar composition.

Table 6
Detailed composition (g Nm^{-3}) of the tar obtained with calcined olivine and Fe/olivine catalyst.

Tar compound	Olivine g Nm^{-3}	Fe/olivine g Nm^{-3}
Light aromatics	**2.99**	**2.08**
Toluene	2.99	2.08
Heterocycles	**2.17**	**0.78**
Phenol	0.66	0.30
Methyl phenol	1.51	0.48
Light PAHs	**13.04**	**6.81**
Indene	0.16	0.00
Naphthalene	6.80	3.97
1-Methyl naphthalene	0.33	0.16
2-Methyl naphthalene	0.31	0.27
Biphenyl	0.18	0.13
Biphenylene	1.47	0.58
Dibenzofuran	0.75	0.22
Fluorene	0.41	0.18
1-H-Phenalene	0.56	0.20
Anthracene	1.32	0.90
Phenanthrene	0.24	0.12
2-Phenyl naphthalene	0.49	0.08
Heavy PAHs	**2.14**	**0.53**
Pyrene	0.82	0.24
Fluoranthene	1.08	0.29
4H-Cyclopenta[def]phenanthrene	0.23	0.00

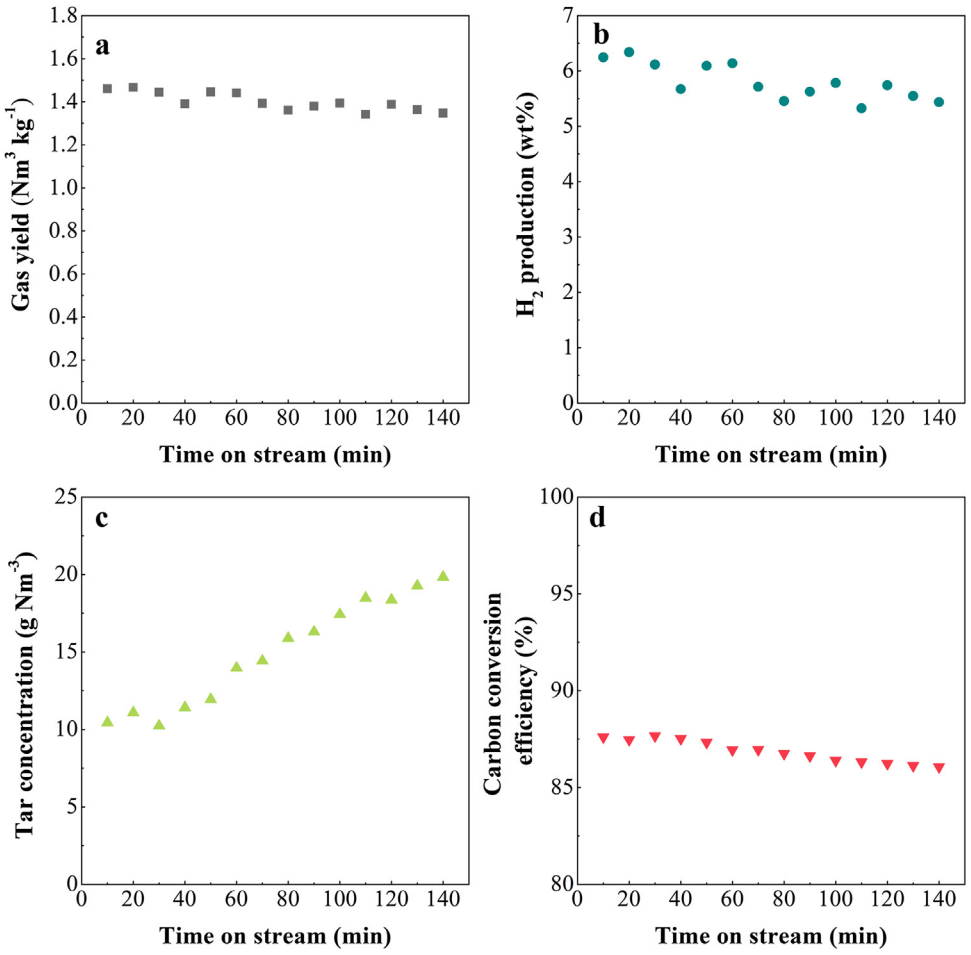

Fig. 8. The evolution of gas production (a), H_2 production (b), tar concentration (on a dry basis) (c) and carbon conversion efficiency (d) with time on stream for Fe/olivine catalyst.

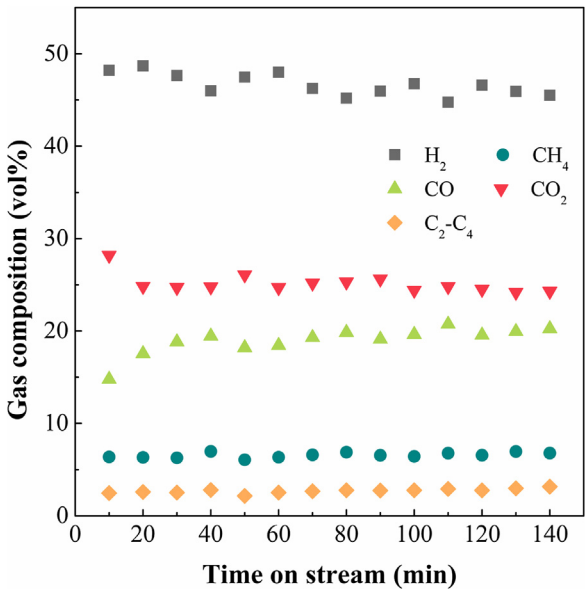

Fig. 9. Gas composition as a function of time on the Fe/olivine catalyst.

Thus, gas and H_2 productions declined from 1.46 $Nm^3 kg^{-1}$ and 6.25 wt% to 1.35 $Nm^3 kg^{-1}$ and 5.44 wt%, respectively (Fig. 8a and b). However, the gas and H_2 productions were still above those obtained with calcined olivine, which suggests that although the catalyst was not able to maintain its original tar elimination capacity, it was still active in the WGS reaction. Likewise, a similar trend was observed in the evolution of the gas composition (Fig. 9). H_2 concentration slightly decreased from 48.2 to 45.5 vol%, whereas that of CO increased from 14.3 to 20.2 vol%. CO_2 concentration remained almost stable at 24.9 vol%. A comparison of this performance with the stable calcined olivine shows that higher H_2 and CO_2 concentrations were obtained, whereas the value of CO was lower due to the enhancement of the WGS reaction. Concerning CH_4 and C_2–C_4 light hydrocarbons, they showed a slightly upward trend. In the case of the deactivated catalyst, CH_4 concentration was even lower (6.4 vol%) than that obtained with the calcined olivine and C_2–C_4 concentration reached a similar value as that with the calcined olivine (2.7 vol %). The latter results are evidence that the Fe/olivine catalyst was still active for steam reforming of CH_4 subsequent to 140 min on stream.

The evolution of tar lumps with time on stream is shown in Fig. 10. As the Fe/olivine catalyst was deactivated, the amount of each tar family was similar to that obtained with the calcined olivine. Thus, the amount of light aromatics and PAHs declined from 19.91 and 64.36 to 15.24 and 57.47 wt%, whereas that of heterocycles and heavy PAHs increased from 7.43 and 5.05 to 10.82 and 11.63 wt% after 140 min on stream. Small differences were observed in the amount of light PAHs between the value with the calcined olivine and that with the deactivated Fe/olivine catalyst, which are related to the amount of unidentified compounds (there were more unidentified compounds with the deactivated catalyst).

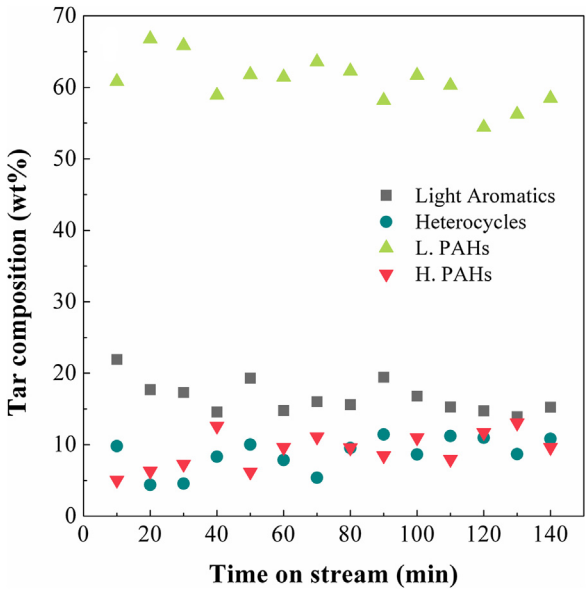

Fig. 10. Tar composition with time on stream on the Fe/olivine catalyst.

When the deactivation of the catalyst was not considerable, the Fe/olivine catalyst seemed to hinder the growth of light PAHs into heavier ones, and the amount of the light PAHs was therefore higher than for the calcined olivine. Moreover, Diels–Alder reactions involving light alkenes in the permanent gases and heterocyclic compounds may also have produced light aromatics, which led to an increase in their amount [96–98].

Table 7
Properties of the fresh and deactivated catalysts.

Catalyst	S_{BET} ($m^2\,g^{-1}$)	V_{pore} ($cm^3\,g^{-1}$)	d_{pore} (Å)
	Fresh/deact.	*Fresh/deact.*	*Fresh/deact.*
Olivine	1.92	0.0003	78.33
Fe/olivine	3.75/2.47	0.0076/0.0021	80.85/34.76

Catalyst deactivation

The prevention and attenuation of catalyst deactivation is a challenging task. Thus, most catalytic processes undergo catalyst deactivation, and therefore understanding the deactivation mechanisms is vital. In the biomass gasification processes, deactivation is mainly caused by sulphur and chlorine poisoning or carbon deposition. However, catalyst physical changes, such as sintering, phase change and attrition may also lead to catalyst deactivation. The deactivated catalyst was characterized in detail in order to understand the main causes of catalyst activity decay.

Table 7 shows the values of the physical properties for the fresh and deactivated Fe/olivine catalysts. After 140 min on stream, the specific surface area of the Fe/olivine catalyst was significantly lower, with the reduction being even more noticeable in the pore volume and size, which underwent a more severe decrease. Therefore, the pores of the catalyst were partially blocked, which led to a decrease in the total surface area, as well as pore volume and size. The deactivated Fe/olivine catalyst had still a higher surface area and pore volume than the calcined olivine. However, the pore size was higher in the calcined olivine.

In order to assess the changes in the metallic structure of the Fe/olivine catalyst after the reaction, Fig. 11 shows the XRD patterns of the reduced and deactivated catalysts. After the reaction, the main crystalline structures were still the olivine structure and the $MgSiO_3$ enstatite phase, although more diffraction lines corresponding to $MgSiO_3$ phase appeared in the deactivated catalyst. The most significant differences between both spectra are related to the iron phases. In the spectrum of the deactivated catalyst, there is no evidence of the presence of metallic iron, neither in $2\theta = 45°$ nor $2\theta = 65°$ diffraction lines. However, multiple lines of Fe_3O_4 or $MgFe_2O_4$ spinel phase were noticeable, which are evidence of a loss of active phase by oxidation of the metallic iron under reaction conditions. Virginie et al. [50] also reported the presence of intense diffraction lines corresponding to Fe_3O_4 or $MgFe_2O_4$ spinel phase after reaction.

XPS analysis of the deactivated catalyst was carried out to determine the components located on the surface of the catalyst after reaction. The XPS spectra of the reduced and deactivated samples in different binding energy ranges are shown in Fig. 12. This analysis revealed that, after the reaction, the main components on the surface of the samples were still Si, Mg, Fe and O (Fig. 12b). However, the presence of K and Ca was also observed, although the amount of the latter on the surface could not be

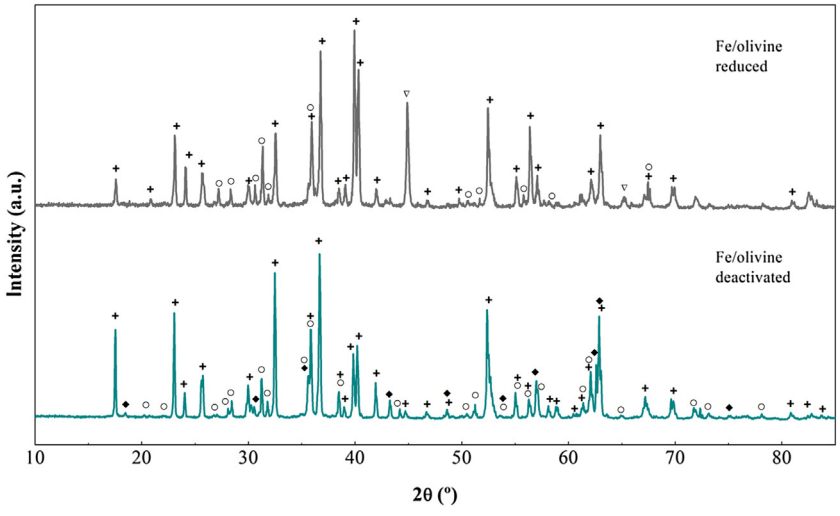

Fig. 11. XRD patterns of reduced and deactivated catalysts. Crystalline phases: (+) $((Mg_{1.81}\cdot Fe_{0.19})\cdot(SiO_4))$, (o) $MgSiO_3$, (▽) Fe°, (◆) Fe_3O_4 or $MgFe_2O_4$ spinel phase.

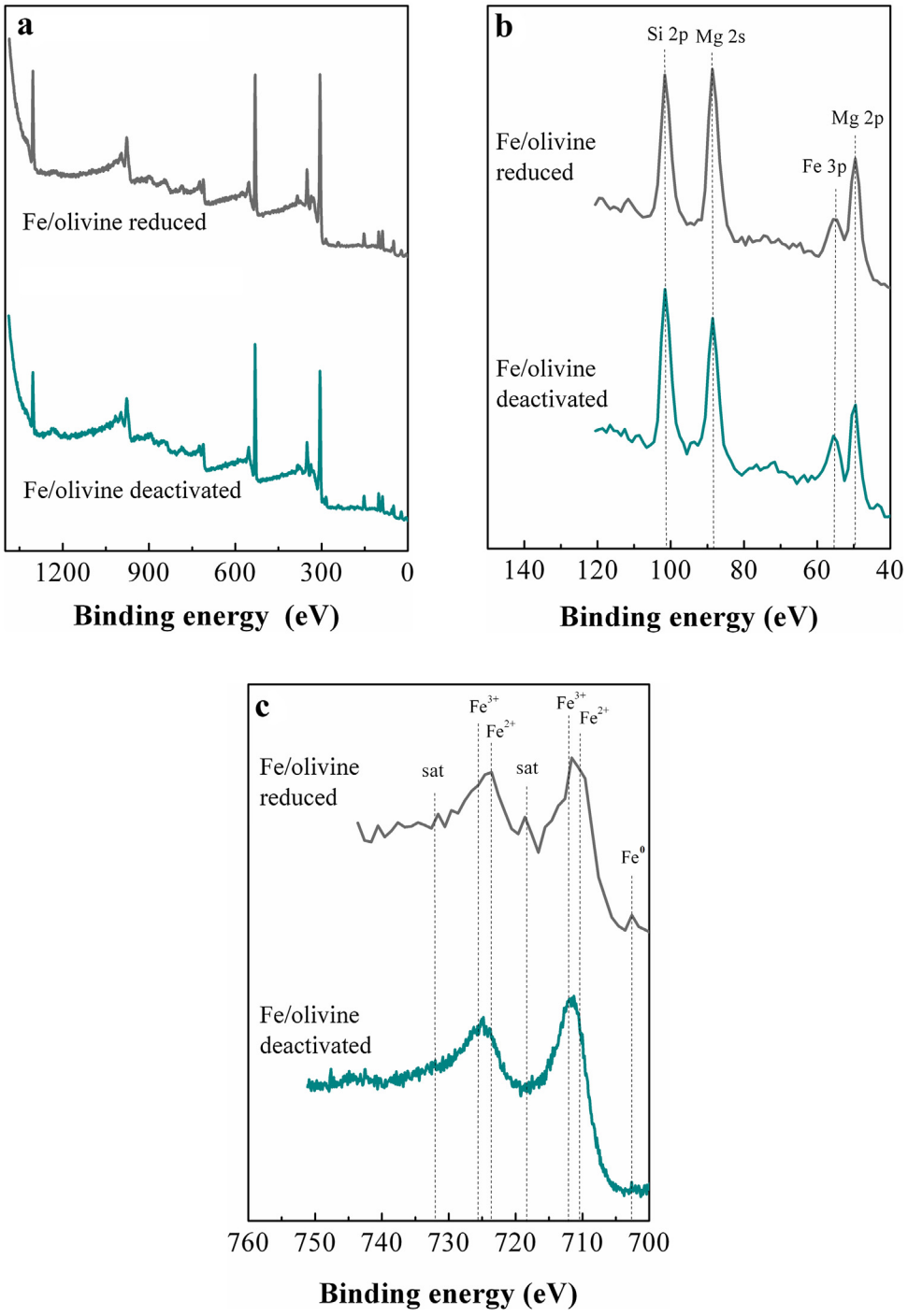

Fig. 12. Wide XPS spectra (a), XPS spectra for low binding energy regions (b) and Fe 2p (d) of the reduced Fe/olivine and deactivated catalysts.

quantified because it was very small. Their existence is probably due to the biomass ashes. As shown in Fig. 12c, metallic iron was not detected on the catalyst surface in the deactivated catalyst, which is consistent with the previous XRD results (Fig. 11).

The surface composition and iron distribution in the reduced and deactivated catalysts are shown in Table 8. As observed, after the reaction there were small differences in the amount of Mg and Fe on the catalyst surface. The amount of iron slightly increased from 4.4 to 5.1% at the expense of Mg, which decreased from 22.1 to 18.4%. However, the iron distribution remained constant (the amount of Fe^{2+} and Fe^{3+} compounds was the same), which is an indication that iron migration from the olivine structure into the surface happened. A comparison of this catalyst with the calcined olivine shows that the deactivated catalyst had more iron in the olivine structure and a higher amount of Fe^{2+} compounds on its surface. Iron migration from the inside to the surface or vice versa

Table 8
Surface composition (%) and iron distribution (%) in the reduced and deactivated Fe/olivine catalysts determined by XPS.

Component	Si	Mg	O	Fe	K	Fe^{2+}/Fe^{3+}
Fe/olivine reduced	14.6	22.1	58.9	4.4	–	1
Fe/olivine deactivated	15.4	18.4	59.8	5.1	1.4	1

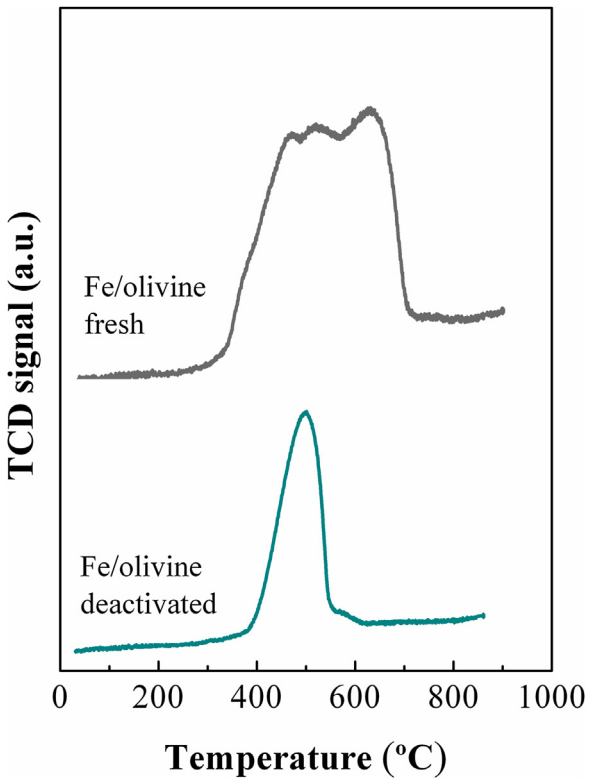

Fig. 13. TPR profiles of the fresh and deactivated catalysts.

occurs in order to reach iron equilibrium in the structure [50,73]. Regarding the amount of K on the deactivated catalyst surface (1.4%), its origin is attributed to biomass ashes. Alvarez et al. [100] reported the chemical analysis of the ashes of the same biomass used in this work and the amount of K_2O was 11.3 wt%. Moreover, at 850 °C, potassium salts melt and they might have formed deposits on the deactivated catalyst surface.

Fig. 13 shows the TPR curve of the fresh and spent catalysts. A single peak at 500 °C with a small shoulder at a slightly higher temperature (590° C) was observed for the deactivated catalyst, which is evidence that the iron in the Fe/olivine catalyst was oxidized during the gasification process. As the XRD revealed, this peak should be attributed to the Fe_3O_4 or $MgFe_2O_4$ spinel phase detected. According to Meng et al. [72], the difficulty for reducing the possible iron oxides is as follows: $MgFe_2O_4 > FeO > Fe_3O_4 > Fe_2O_3$. However, the low reduction temperature suggests that this specie was easy to reduce, i.e., it was probably Fe_3O_4. Furthermore, the shoulder at 590 °C is attributed to the reduction of a small amount of $MgFe_2O_4$ spinel phase. In fact, it seems that most of the $MgFe_2O_4$ spinel phase did not undergo oxidization during the reaction, as it is a very stable compound.

As carbon deposition may cause catalyst deactivation, temperature programmed oxidation (TPO) was conducted on the spent Fe/olivine catalyst to quantify the amount of carbon settled. The total amount of coke and its composition depend on the operating conditions, mainly temperature and S/B ratio, as carbon deposition is a consequence of a balance between its formation and removal by gasification [101]. The TPO analysis revealed that a negligible amount of coke (0.11 wt%) was deposited on the catalyst after the reaction, which is evidence that high temperatures and steam promoted the oxidation of almost all the carbon that may have formed. Fig. 14 shows the TPO profile of the deactivated catalyst. Two different peaks are observed, which is an indication of the heterogeneous nature of the coke. According to the literature

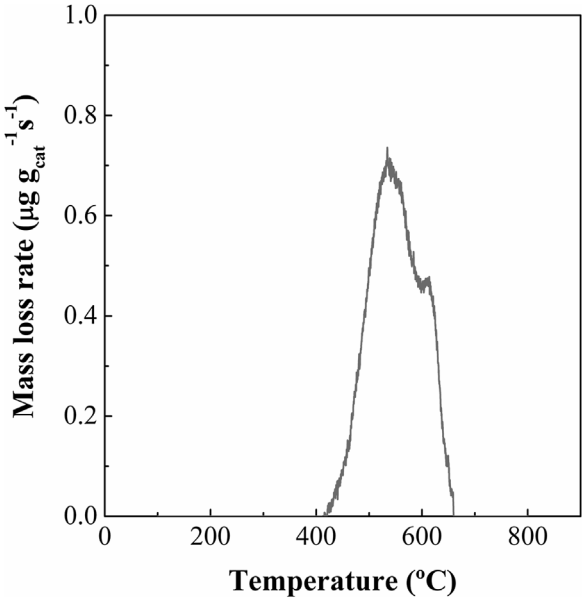

Fig. 14. TPO profile of the deactivated Fe/olivine catalyst.

[102–105], the coke combustion temperature on supported metal catalysts is related to its location on the catalyst and composition. Low combustion temperatures are attributed to the coke deposited on the metallic sites (encapsulating coke), which may catalyse coke combustion, whereas higher combustion temperatures indicate that the coke is deposited on the support, which prevents coke combustion by metallic sites. Furthermore, even if the coke is deposited on similar locations, its combustion temperature is higher as the condensation degree is higher, i.e., more organized structures with lower H/C ratios.

Fig. 14 reveals the heterogeneity of the coke. Thus, two different carbon species were detected, with their combustion temperatures being 530 and 606 °C. The peak at 530 °C is attributed to the amorphous coke and the shoulder at 606 °C to a coke with a slightly more condensate structure. It seems that the severe reaction conditions prevent coke formation from the evolving compounds to more condensed ones due to the in situ gasification of the amorphous coke. Virginie et al. [50] observed a similar TPO profile after biomass steam gasification experiments, although their carbon oxidation temperatures were slightly higher than those obtained in this work (585 and 630 °C). As the coke content was very low (0.11 wt%), it cannot be stated that coke deposition caused catalyst deactivation.

Table 9 shows the chemical composition of the fresh and deactivated Fe/olivine catalysts. XRF analysis revealed that there was no any iron loss due to attrition phenomena, which was also checked by sieving the deactivated catalyst (it had the same size range (90–150 μm) as prior to the runs). Claude et al. [51] and Meng et al. [106] reported that the olivine catalysts synthesized by wet impregnation may undergo attrition, since the metallic species were mainly placed on the surface, and therefore their interaction with the support was rather weak. Some other authors studied this aspect. Thus, Virginie et al. [50] reported an iron loss of 32% after 12 h gasification in a dual fluidized bed and Rapagnà et al. [49] about 5 wt% during 320 min operation in a fluidized bed reactor.

Discussion

The gas composition in the gasifier plays a crucial role on the oxidation state of the iron located on the catalyst. During biomass steam gasification, the metallic Fe^0 was oxidized as detected by XRD, XPS and TPR analyses. The operating methodology used in

Table 9
Chemical composition (wt%) of the fresh and deactivated Fe/olivine catalysts.

Component (wt%)	MgO	SiO_2	Fe_2O_3	CaO	Al_2O_3	Na_2O	TiO_2	MnO
Fe/olivine fresh	42.08	38.68	14.71	0.12	0.24	0.06	0.02	0.10
Fe/olivine deactivated	42.58	39.60	14.30	0.14	0.21	0.07	0.04	0.11

this study had some limitations, which may have contributed to the catalyst oxidation, as explained in the experimental section. These limitations caused changes in the reaction environment, as the fluidizing agent had to be changed from N_2 to steam and ensure suitable fluidization regime prior to starting biomass feed. Thus, the presence of steam may have induced partial oxidation of the metallic phase at the beginning of the reactions. However, as biomass was fed into the reactor, the reaction environment shifted from oxidizing to reducing due to the high hydrogen concentration, and therefore the iron oxidized under steam atmosphere was reduced again. It should be noted that this problem can be avoided in full scale operation with continuous biomass feed.

A similar catalyst deactivation cause was observed in the in-line steam reforming of biomass fast pyrolysis volatiles using 10 wt% Co/Al_2O_3 catalyst by Santamaria et al. [107]. Nordgreen et al. [99] reported that, when the oxygen concentration in the reaction environment is too high, it would oxidize the metallic iron to wustite (FeO) and subsequently to magnetite (Fe_3O_4), since some locations favour these transformations. Based on the results obtained, when Fe was in the metallic state in the Fe/olivine catalyst, it showed a higher activity for reducing tar than when it was in the oxidized state (Fig. 8c). Changes in tar removal capacity of the Fe/olivine catalyst with time on stream may also be related to the distribution of iron oxides. Nordgreen et al. [99] also stated that the catalyst with metallic iron was capable of reducing the tar concentration above 60%, whereas the catalyst with the oxidized iron only had a capacity of 18%. The catalytic activity of iron oxides species increases with their reduction state ($Fe_2O_3 < Fe_3O_4 < FeO < Fe^0$) [51]. After 140 min on stream, the tar concentration obtained with the deactivated Fe/olivine catalyst and that obtained with the calcined olivine were almost the same, which suggests the presence of iron oxides leads to the same tar removal performance as calcined olivine. The same trend was observed in the evolution of tar lumps. As the Fe/olivine catalyst was deactivated, the amount of each tar family was similar to that obtained with the calcined olivine. Undoubtedly, the oxidation of metallic Fe^0 sites led to their decrease, and therefore caused catalyst deactivation, as was revealed by the characterization techniques.

Several studies pointed out that different Fe-phases may catalyze different reactions. Thus, Fe_2O_3 is reported to catalyze shoot and NO_x conversion, Fe_3O_4 to be active in the WGS reaction and metallic Fe to catalyze Boudard reaction and tar removal reactions. Therefore, changes in the oxidation state of iron will drastically influence catalytic properties [73]. However, it seems that, after 140 min on stream, the Fe/olivine catalyst was still active for WGS and CH_4 steam reforming reactions, as shown in Figures 8a and 8b, which may be attributed to Fe_3O_4 or $MgFe_2O_4$ spinel phase detected on the deactivated catalyst (Fig. 11). However, the TPR analysis of the deactivated catalyst was more conclusive than XRD and XPS analyses, which allows inferring that Fe_3O_4 is the responsible, as the reduction temperature was rather low. Some authors proved Fe_3O_4 was active in the WGS reaction [57,58,108–110].

Conclusions

The fountain confined conical spouted bed performs well in the biomass steam gasification with primary catalysts. In fact, this reactor allows enhancing the gas-solid contact, and therefore the catalytic activity by avoiding the elutriation of fine catalyst particles.

Iron incorporation to olivine proved to be beneficial in the biomass steam gasification at zero time on stream, as it allowed not only reducing tar formation, but also improving syngas production and composition. Thus, gas production was increased from 1.30 $Nm^3 kg^{-1}$ with calcined olivine to 1.46 $Nm^3 kg^{-1}$ with Fe/olivine catalyst, and similarly did the hydrogen production, with the value being 6.25 wt%. Likewise, tar concentration was reduced approximately to half, from 20.6 to 11.4 g Nm^3. This was explained by the positive effect of metallic iron, which greatly favours WGS and light hydrocarbon steam reforming and cracking reactions. At zero time on stream, naphthalene was the most abundant tar compound for both the calcined olivine and Fe/olivine catalyst, although its concentration decreased to 42 wt% with the latter.

The evolution of the gasification performance and gas and tar compositions with time on stream was also monitored. The stability of the Fe/olivine catalyst was lower than that of calcined olivine, which was still stable after 140 min on stream. Catalyst deactivation was especially evident based on the tar concentration, which increased from 10.4 to 19.9 g Nm^{-3}, i.e., it almost reached the value obtained on the calcined olivine (20.6 g Nm^{-3}). Other reaction indexes also showed the deterioration of the catalyst. Thus, gas and H_2 productions declined from 1.46 $Nm^3 kg^{-1}$ and 6.25 wt% to 1.35 $Nm^3 kg^{-1}$ and 5.44 wt%, respectively, but still remained above those obtained with the calcined olivine, suggesting the activity of the deactivated Fe/olivine catalyst for WGS and steam reforming of CH_4.

The characterization techniques revealed that the catalyst deactivation was due to the oxidation of the metallic iron into Fe_3O_4. The presence of steam in the reactor for a few minutes before starting biomass feed may have induced the partial oxidation of the metallic phase at the beginning of the reactions. However, as biomass feed started, the reaction environment shifted from oxidizing to reducing conditions, and the iron that may have oxidized became reduced again. These changes in the iron oxidation state had a great influence on the catalytic properties of the Fe/olivine, and therefore on the evolution of tar removal, as well on WGS and light hydrocarbon reforming reactions.

Although the experimental unit used in this study involves certain limitations for the operation with metallic catalysts during the start-up period, the results obtained shed light on the biomass steam gasification using Fe/olivine as primary catalyst in large-scale plants.

Conflict of interest

The authors declare that they have no known competing financial interests or personal relationships that could have appeared to influence the work reported in this paper.

Declaration of Competing Interest

The authors report no declarations of interest.

Acknowledgments

This work was carried out with financial support from the Spain's Ministries of Science, Innovation and Universities (<GN1>RTI2018-098283-J-I00</GN10> (MCIU/AEI/FEDER, UE) and Science and Innovation (PID2019-107357RB-I00 (MCI/AEI/FEDER, UE), the Basque Government (IT1218-19 and KK-2020/00107), and the European Union's Horizon 2020 research and innovation programme under the Marie Skłodowska-Curie grant agreement No. 823745. The authors also thank the technical and human support provided by SGIker from UPV/EHU and European funding (ERDF and ESF).

References

1 A. Molino, V. Larocca, S. Chianese, D. Musmarra, Energies 11 (2018) 811, doi:http://dx.doi.org/10.3390/en11040811.
2 A. Molino, S. Chianese, D. Musmarra, J. Energy Chem. 25 (2016) 10, doi:http://dx.doi.org/10.1016/j.jechem.2015.11.005.
3 I.L. Motta, N.T. Miranda, R.M. Filho, M.R. Wolf Maciel, Renew. Sustain. Energy Rev. 94 (2018) 998, doi:http://dx.doi.org/10.1016/j.rser.2018.06.042.
4 M.A. Salam, K. Ahmed, N. Akter, T. Hossain, B. Abdullah, Int. J. Hydrogen Energy 43 (2018) 14944, doi:http://dx.doi.org/10.1016/j.ijhydene.2018.06.043.
5 N. Hanchate, S. Ramani, C.S. Mathpati, V.H. Dalvi, J. Clean. Prod. 280 (2021) 123148, doi:http://dx.doi.org/10.1016/j.jclepro.2020.123148.
6 Q. He, Q. Guo, K. Umeki, L. Ding, F. Wang, G. Yu, Renew. Sustain. Energy Rev. 139 (2021) 110710, doi:http://dx.doi.org/10.1016/j.rser.2021.110710.
7 S. Anis, Z.A. Zainal, Renew. Sustain. Energy Rev. 15 (2011) 2355, doi:http://dx.doi.org/10.1016/j.rser.2011.02.018.
8 N. Rakesh, S. Dasappa, Renew. Sustain. Energy Rev. 91 (2018) 1045, doi:http://dx.doi.org/10.1016/j.rser.2018.04.017.
9 J. Ren, Y. Liu, X. Zhao, J. Cao, Energy Inst. 93 (2019) 1083, doi:http://dx.doi.org/10.1016/j.joei.2019.10.003.
10 J. Ren, J. Cao, X. Zhao, F. Yang, X. Wei, Renew. Sustain. Energy Rev. 116 (2019), doi:http://dx.doi.org/10.1016/j.rser.2019.109426.
11 A. Larsson, M. Kuba, T. Berdugo Vilches, M. Seemann, H. Hofbauer, H. Thunman, Fuel Process. Technol. 212 (2021) 106609, doi:http://dx.doi.org/10.1016/j.fuproc.2020.106609.
12 J. Yu, Q. Guo, Y. Gong, L. Ding, J. Wang, G. Yu, Fuel Process. Technol. 214 (2021) 106723, doi:http://dx.doi.org/10.1016/j.fuproc.2021.106723.
13 A. Erkiaga, G. Lopez, M. Amutio, J. Bilbao, M. Olazar, Chem. Eng. J. 237 (2014) 259, doi:http://dx.doi.org/10.1016/j.cej.2013.10.018.
14 A. Erkiaga, G. Lopez, M. Amutio, J. Bilbao, M. Olazar, Fuel Process. Technol. 116 (2013) 292, doi:http://dx.doi.org/10.1016/j.fuproc.2013.07.008.
15 A. Pablos, R. Aguado, M. Tellabide, H. Altzibar, F.B. Freire, J. Bilbao, M. Olazar, Powder Technol. 328 (2018) 38, doi:http://dx.doi.org/10.1016/j.powtec.2017.12.090.
16 M. Tellabide, I. Estiati, A. Pablos, H. Altzibar, R. Aguado, M. Olazar, Chem. Eng. Sci. 211 (2020) 115255, doi:http://dx.doi.org/10.1016/j.ces.2019.115255.
17 H. Altzibar, I. Estiati, G. Lopez, J.F. Saldarriaga, R. Aguado, J. Bilbao, M. Olazar, Powder Technol. 312 (2017) 334, doi:http://dx.doi.org/10.1016/j.powtec.2017.01.071.
18 G. Lopez, M. Cortazar, J. Alvarez, M. Amutio, J. Bilbao, M. Olazar, Fuel 203 (2017) 825, doi:http://dx.doi.org/10.1016/j.fuel.2017.05.014.
19 M. Cortazar, G. Lopez, J. Alvarez, M. Amutio, J. Bilbao, M. Olazar, Energy 153 (2018) 455, doi:http://dx.doi.org/10.1016/j.energy.2018.04.067.
20 M. Cortazar, J. Alvarez, G. Lopez, M. Amutio, L. Santamaria, J. Bilbao, M. Olazar, Energy Convers. Manage. 171 (2018) 1589, doi:http://dx.doi.org/10.1016/j.enconman.2018.06.071.
21 M. Tellabide, I. Estiati, A. Atxutegi, H. Altzibar, R. Aguado, M. Olazar, J. Ind. Eng. Chem. 95 (2021) 312, doi:http://dx.doi.org/10.1016/j.jiec.2021.01.006.
22 M.L. Valderrama Rios, A.M. González, E.E.S. Lora, O.A. Almazán del Olmo, Biomass Bioenergy 108 (2018) 345, doi:http://dx.doi.org/10.1016/j.biombioe.2017.12.002.
23 V. Claude, C. Courson, M. Köhler, S.D. Lambert, Energy Fuels 30 (2016) 8791, doi:http://dx.doi.org/10.1021/acs.energyfuels.6b01642.
24 L. Devi, K.J. Ptasinski, F.J.J.G. Janssen, Biomass Bioenergy 24 (2003) 125, doi:http://dx.doi.org/10.1016/S0961-9534(02)00102-2.
25 Y. Shen, K. Yoshikawa, Renew. Sustain. Energy Rev. 21 (2013) 371, doi:http://dx.doi.org/10.1016/j.rser.2012.12.062.
26 A. Arregi, M. Amutio, G. Lopez, J. Bilbao, M. Olazar, Energy Convers. Manage. 165 (2018) 696, doi:http://dx.doi.org/10.1016/j.enconman.2018.03.089.
27 K. Fürsatz, J. Fuchs, F. Benedikt, M. Kuba, H. Hofbauer, Energy 219 (2021) 119650, doi:http://dx.doi.org/10.1016/j.energy.2020.119650.
28 R.S. Tan, T.A. Tuan Abdullah, A. Johari, K. Md Isa, Front. Energy 14 (2020) 545, doi:http://dx.doi.org/10.1007/s11708-020-0800-2.
29 S. Rapagnà, N. Jand, A. Kiennemann, P.U. Foscolo, Biomass Bioenergy 19 (2000) 187, doi:http://dx.doi.org/10.1016/S0961-9534(00)00031-3.
30 S. Koppatz, C. Pfeifer, H. Hofbauer, Chem. Eng. J. 175 (2011) 468, doi:http://dx.doi.org/10.1016/j.cej.2011.09.071.
31 J. Corella, J.M. Toledo, R. Padilla, Energy Fuels 18 (2004) 713, doi:http://dx.doi.org/10.1021/ef0340918.
32 J.M. de Andrés, A. Narros, M.E. Rodríguez, Fuel 90 (2011) 521, doi:http://dx.doi.org/10.1016/j.fuel.2010.09.043.
33 Z. Abu El-Rub, E.A. Bramer, G. Brem, Ind. Eng. Chem. Res. 43 (2004) 6911, doi:http://dx.doi.org/10.1021/ie0498403.
34 E. Gusta, A.K. Dalai, M.A. Uddin, E. Sasaoka, Energy Fuels 23 (2009) 2264, doi:http://dx.doi.org/10.1021/ef8009958.
35 N.M. Nguyen, F. Alobaid, B. Epple, Renew. Energy 172 (2021) 34, doi:http://dx.doi.org/10.1016/j.renene.2021.03.006.
36 H. Li, Y. Wang, N. Zhou, L. Dai, W. Deng, C. Liu, Y. Cheng, Y. Liu, K. Cobb, P. Chen, R. Ruan, J. Clean. Prod. 291 (2021) 125826, doi:http://dx.doi.org/10.1016/j.jclepro.2021.125826.
37 T. Wang, J. Chang, P. Lv, J. Zhu, Energy Fuels 19 (2005) 22, doi:http://dx.doi.org/10.1021/ef030116r.
38 Z. Zhao, N. Lakshminarayanan, J.N. Kuhn, A. Senefeld-Naber, L.G. Felix, R.B. Slimane, C.W. Choi, U.S. Ozkan, Appl. Catal. A 363 (2009) 64, doi:http://dx.doi.org/10.1016/j.apcata.2009.04.042.
39 D. Świerczyński, S. Libs, C. Courson, A. Kiennemann, Appl. Catal. B 74 (2007) 211, doi:http://dx.doi.org/10.1016/j.apcatb.2007.01.017.
40 Q.M.K. Waheed, C. Wu, P.T. Williams, J. Energy Inst. 89 (2016) 657, doi:http://dx.doi.org/10.1016/j.joei.2015.05.006.
41 J.N. Kuhn, Z. Zhao, A. Senefeld-Naber, L.G. Felix, R.B. Slimane, C.W. Choi, U.S. Ozkan, Appl. Catal. A 341 (2008) 43, doi:http://dx.doi.org/10.1016/j.apcata.2007.12.037.
42 C. Zhang, Z. Li, X. Xu, L. Yang, R. Zhang, Adv. Mater. Res. 666 (2013) 67, doi:http://dx.doi.org/10.4028/www.scientific.net/AMR.666.67.
43 H. Sun, J. Wang, J. Zhao, B. Shen, J. Shi, J. Huang, C. Wu, Appl. Catal. B 244 (2019) 63, doi:http://dx.doi.org/10.1016/j.apcatb.2018.11.040.
44 A. Farooq, S. Moogi, S. Jang, H.P.R. Kannapu, S. Valizadeh, A. Ahmed, S.S. Lam, Y. Park, J. Ind. Eng. Chem. 94 (2021) 336, doi:http://dx.doi.org/10.1016/j.jiec.2020.11.005.
45 Y. Pan, A. Abulizi, D. Talifu, Y. Tursun, S. Xu, Fuel Process. Technol. 194 (2019) 106121, doi:http://dx.doi.org/10.1016/j.fuproc.2019.106121.
46 C. Quan, S. Xu, C. Zhou, Energy Convers. Manage. 141 (2017) 40, doi:http://dx.doi.org/10.1016/j.enconman.2016.04.024.
47 M. Virginie, C. Courson, A. Kiennemann, C.R. Chim. 13 (2010) 1319, doi:http://dx.doi.org/10.1016/j.crci.2010.03.022.
48 M. Virginie, C. Courson, D. Niznansky, N. Chaoui, A. Kiennemann, Appl. Catal. B 101 (2010) 90, doi:http://dx.doi.org/10.1016/j.crci.2010.03.022.
49 S. Rapagnà, M. Virginie, K. Gallucci, C. Courson, M. Di Marcello, A. Kiennemann, P.U. Foscolo, Catal. Today 176 (2011) 163, doi:http://dx.doi.org/10.1016/j.cattod.2010.11.098.
50 M. Virginie, J. Adánez, C. Courson, L.F. De Diego, F. García-Labiano, D. Niznansky, A. Kiennemann, P. Gayán, A. Abad, Appl. Catal. B 121–122 (2012) 214, doi:http://dx.doi.org/10.1016/j.apcatb.2012.04.005.
51 V. Claude, J.G. Mahy, S. Douven, S.L. Pirard, C. Courson, S.D. Lambert, Mater. Today Chem. 14 (2019) 100197, doi:http://dx.doi.org/10.1016/j.mtchem.2019.100197.
52 I. Zamboni, C. Courson, A. Kiennemann, Appl. Catal. B 203 (2017) 154, doi:http://dx.doi.org/10.1016/j.apcatb.2016.10.024.
53 T. Xu, F. Xu, G.G. Moyo, Y. Sun, Z. Chen, B. Xiao, X. Wang, Z. Hu, Energy Convers. Manage. 199 (2019) 111937, doi:http://dx.doi.org/10.1016/j.enconman.2019.111937.
54 K. Matsuoka, T. Shimbori, K. Kuramoto, H. Hatano, Y. Suzuki, Energy Fuels 20 (2006) 2727, doi:http://dx.doi.org/10.1021/ef060301f.
55 M. Pudukudy, Z. Yaakob, K. Mhd Syahri, Q. Jia, S. Shan, J. Ind. Eng. Chem. 84 (2020) 150, doi:http://dx.doi.org/10.1016/j.jiec.2019.12.030.
56 J. Dufour, C. Martos, A. Ruiz, Magn. Struct. Prop. Appl. (2011) 209.
57 C. Chou, J.A. Loiland, R.F. Lobo, Catalysts 9 (2019) 773, doi:http://dx.doi.org/10.3390/catal9090773.
58 C. Martos, J. Dufour, A. Ruiz, Int. J. Hydrogen Energy 34 (2009) 4475, doi:http://dx.doi.org/10.1016/j.ijhydene.2008.08.042.
59 J. Alvarez, B. Hooshdaran, M. Cortazar, M. Amutio, G. Lopez, F.B. Freire, M. Haghshenasfard, S.H. Hosseini, M. Olazar, Fuel 224 (2018) 111, doi:http://dx.doi.org/10.1016/j.fuel.2018.03.028.
60 J. Alvarez, M. Amutio, G. Lopez, L. Santamaria, J. Bilbao, M. Olazar, Waste Manage. 85 (2019) 385, doi:http://dx.doi.org/10.1016/j.wasman.2019.01.003.
61 G. Lopez, A. Erkiaga, M. Artetxe, M. Amutio, J. Bilbao, M. Olazar, Ind. Eng. Chem. Res. 54 (2015) 9536, doi:http://dx.doi.org/10.1021/acs.iecr.5b02413.
62 M. Amutio, G. Lopez, J. Alvarez, M. Olazar, J. Bilbao, Bioresour. Technol. 194 (2015) 225, doi:http://dx.doi.org/10.1016/j.biortech.2015.07.030.
63 G. Lopez, A. Erkiaga, M. Amutio, J. Bilbao, M. Olazar, Fuel 153 (2015) 393, doi:http://dx.doi.org/10.1016/j.fuel.2015.03.006.
64 H. Altzibar, G. Lopez, J. Bilbao, M. Olazar, Ind. Eng. Chem. Res. 52 (2013) 2995, doi:http://dx.doi.org/10.1021/ie302407f.
65 I. García-García, E. Acha, K. Bizkarra, J. Martínez de Ilarduya, J. Requies, J.F. Cambra, Int. J. Hydrogen Energy 40 (2015) 14445, doi:http://dx.doi.org/10.1016/j.ijhydene.2015.07.155.
66 L. Santamaria, G. Lopez, A. Arregi, M. Amutio, M. Artetxe, J. Bilbao, M. Olazar, Appl. Catal. B 229 (2018) 105, doi:http://dx.doi.org/10.1016/j.apcatb.2018.02.003.
67 R. Michel, M.R. Ammar, J. Poirier, P. Simon, Ceram. Int. 39 (2013) 5287, doi:http://dx.doi.org/10.1016/j.ceramint.2012.12.031.
68 R. Michel, M.R. Ammar, E. Véron, P. Simon, J. Poirier, RSC Adv. 4 (2014) 26645, doi:http://dx.doi.org/10.1039/c4ra01238k.

69 D. Swierczynski, C. Courson, L. Bedel, A. Kiennemann, S. Vilminot, Chem. Mater. 18 (2006) 897, doi:http://dx.doi.org/10.1021/cm051433.
70 M. Morin, X. Nitsch, S. Pécate, M. Hémati, Fuel 209 (2017) 25, doi:http://dx.doi.org/10.1016/j.fuel.2017.07.084.
71 J.N. Kuhn, Z. Zhao, L.G. Felix, R.B. Slimane, C.W. Choi, U.S. Ozkan, Appl. Catal. B 81 (2008) 14, doi:http://dx.doi.org/10.1016/j.apcatb.2007.11.040.
72 J. Meng, Z. Zhao, X. Wang, J. Chen, A. Zheng, Z. Huang, G. Wei, H. Li, J. Energy Inst. 92 (2019) 1765, doi:http://dx.doi.org/10.1016/j.joei.2018.12.004.
73 H.O.A. Fredriksson, R.J. Lancee, P.C. Thüne, H.J. Veringa, J.W.H. Niemantsverdriet, Appl. Catal. B 130–131 (2013) 168, doi:http://dx.doi.org/10.1016/j.apcatb.2012.10.017.
74 T. Yamashita, P. Hayes, Appl. Surf. Sci. 254 (2008) 2441, doi:http://dx.doi.org/10.1016/j.apsusc.2007.09.063.
75 S. Da Ros, K.A. Valter Flores, M. Schwaab, E. Barbosa-Coutinho, N.R.C. Fernandes, J.C. Pinto, J. Ind. Eng. Chem. 94 (2021) 425, doi:http://dx.doi.org/10.1016/j.jiec.2020.11.018.
76 T. Nordgreen, T. Liliedahl, K. Sjöström, Fuel 85 (2006) 689, doi:http://dx.doi.org/10.1016/j.fuel.2005.08.026.
77 L. Devi, M. Craje, P. Thüne, K.J. Ptasinski, F.J.J.G. Janssen, Appl. Catal. A 294 (2005) 68, doi:http://dx.doi.org/10.1016/j.apcata.2005.07.044.
78 J. Meng, Z. Zhao, X. Wang, X. Wu, A. Zheng, Z. Huang, K. Zhao, H. Li, Int. J. Hydrogen Energy 43 (2018) 127, doi:http://dx.doi.org/10.1016/j.ijhydene.2017.11.037.
79 S. Nam, Y. Park, Y. Yun, J. Gu, H. Sung, M. Horio, Korean J. Chem. Eng. 33 (2016) 465, doi:http://dx.doi.org/10.1007/s11814-015-0159-y.
80 M. Artetxe, J. Alvarez, M.A. Nahil, M. Olazar, P.T. Williams, Energy Convers. Manage. 136 (2017) 119, doi:http://dx.doi.org/10.1016/j.enconman.2016.12.092.
81 M. Artetxe, M.A. Nahil, M. Olazar, P.T. Williams, Fuel 184 (2016) 629, doi:http://dx.doi.org/10.1016/j.fuel.2016.07.036.
82 R.S. Tan, T.A. Tuan Abdullah, A. Abdul Jalil, K. Md Isa, J. Energy Inst. 93 (2020) 1177, doi:http://dx.doi.org/10.1016/j.joei.2019.11.001.
83 X. Zou, T. Chen, P. Zhang, D. Chen, J. He, Y. Dang, Z. Ma, Y. Chen, P. Toloueinia, C. Zhu, J. Xie, H. Liu, S.L. Suib, Appl. Energy 226 (2018) 827, doi:http://dx.doi.org/10.1016/j.apenergy.2018.06.005.
84 E. Savuto, R.M. Navarro, N. Mota, A. Di Carlo, E. Bocci, M. Carlini, J.L.G. Fierro, Fuel 224 (2018) 676, doi:http://dx.doi.org/10.1016/j.fuel.2018.03.081.
85 T. Ahmed, S. Xiu, L. Wang, A. Shahbazi, Fuel 211 (2018) 566, doi:http://dx.doi.org/10.1016/j.fuel.2017.09.051.
86 M.A. Adnan, O. Muraza, S.A. Razzak, M.M. Hossain, H.I. De Lasa, Energy Fuels 31 (2017) 7471, doi:http://dx.doi.org/10.1021/acs.energyfuels.7b01301.
87 J. Cao, J. Ren, X. Zhao, X. Wei, T. Takarada, Fuel 217 (2018) 515, doi:http://dx.doi.org/10.1016/j.fuel.2017.12.121.
88 S. Kim, H. Prajitno, J. Yoo, S. Kim, D. Chun, J. Lim, H. Choi, S. Lee, H. Im, J. Ind. Eng. Chem. 94 (2021) 317, doi:http://dx.doi.org/10.1016/j.jiec.2020.11.002.
89 A. Cavalli, R. Tetteroo, M. Graziadio, P.V. Aravind, Biomass Bioenergy 146 (2021) 105982, doi:http://dx.doi.org/10.1016/j.biombioe.2021.105982.
90 D. Barisano, G. Canneto, F. Nanna, E. Alvino, G. Pinto, A. Villone, M. Carnevale, V. Valerio, A. Battafarano, G. Braccio, Fuel Process. Technol. 141 (2016) 74, doi:http://dx.doi.org/10.1016/j.fuproc.2015.06.008.
91 D. Barisano, C. Freda, F. Nanna, E. Fanelli, A. Villone, Bioresour. Technol. 118 (2012) 187, doi:http://dx.doi.org/10.1016/j.biortech.2012.05.011.
92 C. Pfeifer, R. Rauch, H. Hofbauer, Ind. Eng. Chem. Res. 43 (2004) 1634, doi:http://dx.doi.org/10.1021/ie030742b.
93 R. Michel, S. Rapagnà, M. Di Marcello, P. Burg, M. Matt, C. Courson, R. Gruber, Fuel Process. Technol. 92 (2011) 1169, doi:http://dx.doi.org/10.1016/j.fuproc.2010.12.005.
94 Y. Tursun, S. Xu, A. Abulikemu, T. Dilinuer, Bioresour. Technol. 272 (2019) 241, doi:http://dx.doi.org/10.1016/j.biortech.2018.10.008.
95 M. Cortazar, G. Lopez, J. Alvarez, M. Amutio, J. Bilbao, M. Olazar, Fuel 253 (2019) 1446, doi:http://dx.doi.org/10.1016/j.fuel.2019.05.094.
96 Y. Qin, A. Campen, T. Wiltowski, J. Feng, W. Li, Biomass Bioenergy 83 (2015) 77, doi:http://dx.doi.org/10.1016/j.biombioe.2015.09.001.
97 X. Nitsch, J. Commandré, P. Clavel, E. Martin, J. Valette, G. Volle, Energy Fuels 27 (2013) 5459, doi:http://dx.doi.org/10.1021/ef400817z.
98 J. Meng, Z. Zhao, X. Wang, A. Zheng, D. Zhang, Z. Huang, K. Zhao, G. Wei, H. Li, Energy Convers. Manage. 168 (2018) 60, doi:http://dx.doi.org/10.1016/j.enconman.2018.04.112.
99 T. Nordgreen, V. Nemanova, K. Engvall, K. Sjöström, Fuel 95 (2012) 71, doi:http://dx.doi.org/10.1016/j.fuel.2011.06.002.
100 J. Alvarez, G. Lopez, M. Amutio, J. Bilbao, M. Olazar, Energy Convers. Manage. 181 (2019) 214, doi:http://dx.doi.org/10.1016/j.enconman.2018.12.008.
101 A. Remiro, B. Valle, A.T. Aguayo, J. Bilbao, A.G. Gayubo, Fuel Process. Technol. 115 (2013) 222, doi:http://dx.doi.org/10.1016/j.fuproc.2013.06.003.
102 E. Fernandez, M. Amutio, M. Artetxe, A. Arregi, L. Santamaria, G. Lopez, J. Bilbao, M. Olazar, Process Saf. Environ. Prot. 145 (2021) 52, doi:http://dx.doi.org/10.1016/j.psep.2020.07.039.
103 L. Santamaria, A. Arregi, G. Lopez, M. Artetxe, M. Amutio, J. Bilbao, M. Olazar, Fuel 262 (2020) 116593, doi:http://dx.doi.org/10.1016/j.fuel.2019.116593.
104 A. Ochoa, A. Arregi, M. Amutio, A.G. Gayubo, M. Olazar, J. Bilbao, P. Castaño, Appl. Catal. B 233 (2018) 289, doi:http://dx.doi.org/10.1016/j.apcatb.2018.04.002.
105 A. Arregi, G. Lopez, M. Amutio, I. Barbarias, L. Santamaria, J. Bilbao, M. Olazar, J. Ind. Eng. Chem. 68 (2018) 69, doi:http://dx.doi.org/10.1016/j.jiec.2018.07.030.
106 J. Meng, X. Wang, Z. Zhao, A. Zheng, Z. Huang, G. Wei, K. Lv, H. Li, Bioresour. Technol. 268 (2018) 212, doi:http://dx.doi.org/10.1016/j.biortech.2018.07.135.
107 L. Santamaria, G. Lopez, A. Arregi, M. Artetxe, M. Amutio, J. Bilbao, M. Olazar, J. Ind. Eng. Chem. 91 (2020) 167, doi:http://dx.doi.org/10.1016/j.jiec.2020.07.050.
108 C. Chen, H. Ren, J. Zhou, Y. Luo, Y. Zhan, C. Au, X. Lin, L. Jiang, Int. J. Hydrogen Energy 45 (2020) 8456, doi:http://dx.doi.org/10.1016/j.ijhydene.2020.01.023.
109 Z. Fu, J. Wang, N. Zhang, Y. An, Z. Yang, Int. J. Hydrogen Energy 40 (2015) 2193, doi:http://dx.doi.org/10.1016/j.ijhydene.2014.12.063.
110 C. Ratnasamy, J. Wagner, Catal. Rev. Sci. Eng. 51 (2009) 325, doi:http://dx.doi.org/10.1080/01614940903048661.